

OPEN ACCESS

EDITED BY Rahul Dilawari, University of Texas Medical Branch at Galveston, United States

REVIEWED BY Noha Nafee, Kuwait University, Kuwait Abu Md. Ashif Ikbal, Assam University, India

*CORRESPONDENCE

Yan Luo,

✓ yanluo2018@cqu.edu.cn

[†]These authors have contributed equally to this work

RECEIVED 21 August 2025 REVISED 08 October 2025 ACCEPTED 27 October 2025 PUBLISHED 07 November 2025

CITATION

Li X-Y, Yang Y-N, Xie Y, Huang L, Long Y-Y, Luo Q, Wang C and Luo Y (2025) Triplemodality nanotheranostics for nasopharyngeal carcinoma: porphyrin-driven photothermalchemo-radiosensitization with MRIguided precision.

Front. Nanotechnol. 7:1690060. doi: 10.3389/fnano.2025.1690060

COPYRIGHT

© 2025 Li, Yang, Xie, Huang, Long, Luo, Wang and Luo. This is an open-access article distributed under the terms of the Creative Commons Attribution License (CC BY). The use, distribution or reproduction in other forums is permitted, provided the original author(s) and the copyright owner(s) are credited and that the original publication in this journal is cited, in accordance with accepted academic practice. No use, distribution or reproduction is permitted which does not comply with these terms.

Triple-modality nanotheranostics for nasopharyngeal carcinoma: porphyrin-driven photothermal-chemo-radiosensitization with MRI-guided precision

Xiao-Yu Li^{1†}, Ya-Na Yang^{2†}, Yue Xie¹, Luo Huang¹, Yan-Yan Long¹, Qian Luo¹, Can Wang¹ and Yan Luo^{1*}

¹Radiation Oncology Center, Chongqing University Cancer Hospital, Chongqing, China, ²Health Management Center, The First Affiliated Hospital of Chongqing Medical University, Chongqing, China

Nasopharyngeal carcinoma (NPC) poses significant therapeutic challenges due to its anatomical complexity, hypoxic/fibrotic microenvironment, and high recurrence rates post-chemoradiotherapy, necessitating multifunctional nanoplatforms that overcome resistance and enable precise image-guided therapy. To address this, we developed a multifunctional nanoplatform based on PVA-Ppa, which can be further functionalized through Gd3+ chelation for magnetic resonance imaging (MRI) and radiosensitization, and physically loaded with doxorubicin (DOX) for chemotherapy. Comprehensive characterization assessed physicochemical properties, DOX loading, photothermal efficiency, MRI contrast, and radiosensitization using CNE-2 cells line and CNE-2 xenograft mice. Results demonstrated uniform spherical nanoparticles (36.40 ± 14.67 nm) with high DOX loading capacity (73%) and sustained release. Photothermal irradiation (690 nm) induced rapid temperature rise (>30 °C, P < 0.01) and ROS-mediated apoptosis. Gd-chelation significantly enhanced radiosensitization (sensitization enhancement ratio = 1.69) and radiation-induced apoptosis (40% vs. 17% control). Triple-combination therapy (PVA-Ppa-Gd-DOX + X-ray + laser) achieved complete tumor regression and significantly prolonged survival in vivo. Nanoparticles exhibited high T1 relaxivity (4.17 mM⁻¹s⁻¹ at 7T vs. 1.76 mM⁻¹s⁻¹ for Gd-DTPA), enabling prolonged tumor visualization and real-time therapeutic monitoring. This integrated PVA-Ppa-Gd nanoplatform presents a promising strategy for NPC theranostics, demonstrating potent efficacy in a preclinical model and showing potential to address the challenges of NPC treatment through MRI-guieded precision with synergistic triple-modality therapy. Its translation potential warrants further validation in more complex, orthotopic models.

KEYWORDS

theranostic nanoparticles, nasopharyngeal carcinoma, triple-modality therapy, MRI-guided therapy, synergistic radiosensitization

1 Introduction

Nasopharyngeal carcinoma (NPC) represents a biologically aggressive malignancy with inherent therapeutic resistance, driven by its complex anatomical positioning and association with oncogenic factors such as Epstein-Barr virus infection (Looi et al., 2024; Siak et al., 2023). This tumor's location in proximity to critical neurovascular structures frequently precludes surgical resection, establishing chemoradiotherapy as the principal treatment approach for the vast majority of cases (Alsavaf et al., 2025; Looi et al., 2024). However, the tumor microenvironment, characterized by dense fibrotic stroma and chronic hypoxia, substantially compromises drug delivery and radiation effectiveness (Cai et al., 2024; Lee et al., 2022). These pathophysiological features contribute to persistent locoregional recurrence rates, which remain elevated at approximately 20%-30% despite the utilization of advanced techniques like intensitymodulated radiotherapy (IMRT) (Liang et al., 2025). These persistent therapeutic challenges underscore the critical need for innovative strategies that can simultaneously overcome the biological barriers inherent to NPC while enhancing treatment precision. Nanomedicine offers a promising shift by allowing the design of multifunctional platforms for targeted drug delivery and tumor microenvironment modulation, as well as integrating various therapeutic modalities. Real-time visualization is essential for accurate combinatorial therapy in anatomically complex NPC.

Despite advances in nanomedicine, existing platforms for NPC therapy remain constrained by functional compartmentalization and mechanistic oversimplification. Many nano-platforms prioritize the delivery of a single therapeutic agent or rely heavily on one mechanism of action, such as conventional chemotherapy delivery via nanocarriers (Fang et al., 2023) or singular photodynamic therapy (PDT) (Lin et al., 2023), often neglecting the complex, multifactorial nature of NPC progression and therapeutic resistance. This singular-mode approach frequently overlooks the need for synergistic combination strategies, including the integration of complementary therapeutic modalities like combining PDT with chemoradiotherapy (Wu et al., 2024) that could address NPC more comprehensively. Beyond that, current nanomaterial designs often fail to adequately address the profound heterogeneity of NPC tumors and the diverse, adaptive mechanisms driving treatment resistance like chemoresistance (Huang et al., 2024) and radioresistance (Li et al., 2025; Zhang et al., 2025). Furthermore, the functional compartmentalization often leads to a disconnect between diagnostic and therapeutic capabilities. While theranostics is a major goal, many platforms fail to effectively integrate sensitive diagnostic elements like imaging agents with potent therapeutic functions effectively within a single, unified nano-entity (Wang et al., 2025), resulting in platforms that excel in one aspect but are deficient in the other (Duan et al., 2024). Consequently, advancing nanomedicine for NPC necessitates a more holistic approach that integrates multifunctionality, addresses tumor heterogeneity and complex resistance networks, and demonstrates clear synergistic benefits with standard therapies in clinically relevant models.

Radiotherapy (RT) remains the cornerstone of NPC management due to the tumor's anatomic complexity. The deep

anatomic location and proximity to critical structures necessitate high-precision RT delivery, making image-guided radiotherapy (IGRT) indispensable. IGRT could enhance precision through real-time imaging verification prior to each radiation fraction, thereby mitigating setup errors and anatomic changes while improving tumor targeting consistency during adaptive replanning (Youden et al., 2022). Hence, the employment of suitable medical imaging techniques is of utmost importance. Among the myriad of imaging modalities accessible, magnetic resonance imaging (MRI) emerges as a well-established and pivotal instrument in clinical medicine, attributed to its noninvasive attribute, exceptional spatial resolution, and capability in soft-tissue contrast (Li et al., 2024a; Li et al., 2024b). In recent years, there has been extensive development of contrast agents to augment the imaging capabilities of MRI, as reported in numerous academic publications across various fields. Gadolinium (Gd)-based nanoparticles represent a highly promising class of nanomaterials for MRI image guidance in NPC radiotherapy. These nanoparticles offer superior magnetic resonance imaging properties compared to conventional small molecule Gd chelates. For instance, single-atom Gd nanoprobes (Gd-SA) demonstrated remarkably high relaxivity (r1) of 34.2 mM⁻¹.s⁻¹ at 3T, far exceeding those of commercial Gd chelates like Gd-DTPA (Luo et al., 2023). This enhanced relaxivity directly translates to superior imaging sensitivity and contrast, which is crucial for precisely delineating the primary gross tumor volume in NPC. Moreover, Gd-based nanoparticles provide a wider imaging time window (Liu et al., 2023). Noteworthily, Gd-based nanoparticles offer integrated theranostic capabilities. A recently developed Gd-based theranostic nanoparticle demonstrated its potential in the first-in-human clinical trials, combining imaging with enhanced radiation therapy (Chargari et al., 2024). These nanoparticles act not only as exceptional T1 contrast agents but also leverage the high atomic number (Z) of Gd to function as radiosensitizers (Sun et al., 2022; Garcia-Prada et al., 2023; Liu et al., 2025). The Gd atoms enhance localized radiation dose deposition within the tumor through increased secondary radiation generation following ion beam interaction, improving therapeutic efficacy during IGRT. The integration of imaging agents and multimodal therapeutic agents into a nanoplatform facilitates the precise localization of tumor sites, the determination of tumor dimensions, and the monitoring of the biodistribution of nanoparticles subsequent to drug administration. This area of research holds substantial promise for MRI-guided precision cancer therapy, offering a promising avenue for advancing medical interventions in NPC.

Herein, we present a polyvinyl alcohol-pheophorbide (PVA-Ppa-Gd) a-gadolinium nanocomposite, specifically designed to address these interconnected challenges through the synergistic integration of multiple therapeutic modalities. Essentially, Ppa functions as a hydrophobic anchor for loading DOX and as a photothermal converter, enabling localized hyperthermia when exposed to 690 nm laser irradiation. This generated heat not only directly ablates tumors but also increases vascular permeability, facilitating DOX penetration into dense stromal areas. Concurrently, the Gd3+ ions chelated to Ppa intensify radiation-induced oxidative stress, thereby elevating intracellular ROS levels. The PVA system further coordinates Gd3+ ions to prolong tumor retention, enabling high-resolution

T1-weighted MRI for real-time therapy monitoring. *In vivo* studies demonstrated significant tumor regression with triple-modality therapy, outperforming single-modality controls by >50%. By integrating these functions into a biodegradable scaffold, our platform advances the field of NPC nanotheranostics. It replaces empirical combination therapies with a mechanism-driven system where imaging guides therapy, therapy enhances imaging, and both synergize to overcome biological resistance. This study introduces a novel class of nanocomposites that integrates material innovation with profound biological interactions, addressing unfulfilled clinical requirements.

2 Materials and methods

2.1 Materials

Polyvinyl alcohol (PVA, Molecular Weight = 40,000, 99% hydrolyzed), Pheophorbide a (Ppa, ≥98.0%) and Doxorubicin 99.90%) hydrochloride (DOX, were obtained MedChemExpress (NJ, United States). GdCl₃ (99.99% trace basis), dimethyl sulfoxide (DMSO), N'dicyclohexylcarbodiimide (DCC), 4-dimethylaminopyridine (DMAP), N-hydroxybenzotriazole (HOBT), and Sodium Dodecyl Sulfate (SDS) and ROS-sensitive probe DCFH-DA were sourced from Sigma-Aldrich (MA, United States). RPMI 1640 medium, fetal bovine serum (FBS, heat-inactivated), trypsin-EDTA solution (0.25%, with phenol red) and penicillin-streptomycin (10,000 U/ mL) were obtained from Gibco (NY, United States). MTS assay kit (Abcam, Cambridge, United Kingdom), Annexin V-FITC/PI apoptosis detection kit (BD Biosciences, NJ, United States), and Hoechst 33342 (Thermo Fisher, MA, United States) were employed for functional assays. Additionally, Phosphate-Buffered Saline (PBS) were obtained from Procell (Wuhan, China).

2.2 Cells and animals

Human CNE-2 nasopharyngeal carcinoma cells were purchased from Bioesn (Shanghai, China). The cells were maintained in RPMI 1640 medium supplemented with 10% fetal bovine serum and 1% antibiotics (penicillin and streptomycin) in an atmosphere of 5% CO2 at 37 °C. BALB/c nude mice (4-6 weeks old) were obtained from Beijing Vital River Laboratory (Beijing, China). All mice were housed in individually ventilated cages (IVCs) under specific pathogen-free (SPF) conditions, with environmental conditions maintained at 22 °C \pm 2 °C, 50% \pm 10% humidity, and a 12/12-h light/dark cycle. Standard laboratory rodent diet and autoclaved water were provided ad libitum. Cages contained nesting material and a shelter for environmental enrichment, and were regularly changed in a laminar flow hood to ensure hygiene. For anesthesia, mice received an intraperitoneal injection of pentobarbital (40 mg/kg). Euthanasia was conducted in accordance with the AVMA Guidelines (2020) using carbon dioxide (CO₂) inhalation, wherein a gradually increasing concentration (30%-70%) was applied to induce unconsciousness, followed by 100% CO2 to ensure irreversible cessation of vital functions. All animal procedures were reviewed and approved by the Animal Ethics Committee of Chongqing University Cancer Hospital, in accordance with the guidelines of Chinese national regulations on laboratory animal welfare (GB/T 35823-2018) and local laboratory animal use guidelines issued by the Chongqing Science and Technology Bureau (Permit Number: SYXK (Yu) 2021-0001).

2.3 Synthesis and characterization of PVA-Ppa conjugates

2.3.1 Synthesis and purification

PVA-Ppa conjugates were synthesized through carbodiimidemediated esterification, as previously reported. In brief, PVA (40 kDa) was dissolved in anhydrous DMSO at a concentration of 50 mg/mL under a nitrogen atmosphere (Luo et al., 2017). To this solution, Ppa dissolved in DMSO (2 mg/mL) was added at a molar ratio of 1:100 (PVA: Ppa). The reaction mixture was then activated using N, N'-dicyclohexylcarbodiimide (DCC), 4-dimethylaminopyridine (DMAP), and N-hydroxybenzotriazole (HOBT). The reaction proceeded with continuous stirring at 500 rpm at room temperature for 48 h, protected from light. The crude product was precipitated by the dropwise addition of ice-cold ethanol (5 reaction volumes, -20 °C), followed by centrifugation at 10,000×g for 15 min at 4 °C. The pellet was washed three times with ethanol/water (v/v 9:1) and redissolved in DMSO. Purification was achieved by dialyzing against deionized water for 48 h with six solvent exchanges. The final product was lyophilized and stored in a desiccated state at -20 °C.

2.3.2 Chemical structure verification

The chemical structure of the PVA-Ppa conjugate was verified using ¹H NMR spectroscopy (Quantum-I Plus 400 MHz, Zhongke-Niujin, China) with DMSO as the solvent. Further confirmation was obtained by Fourier-transform infrared (FTIR) spectroscopy (IR Tracer-100, Shimadzu, Japan) using the attenuated total reflectance mode. The amount of conjugated Ppa was quantified spectrophotometrically. A calibration curve was established by plotting the absorbance of Ppa standards at 680 nm against their concentrations. The Ppa loading content in the conjugate was determined against this curve.

2.3.3 Nanoparticle size, morphology, and zeta potential

The covalent conjugation of hydrophobic Ppa to the hydrophilic PVA backbone confers an amphiphilic character to the PVA-Ppa conjugate, enabling it to self-assemble into core-shell nanoparticles in aqueous environments. The self-assembly capability was quantitatively assessed by measuring the critical micelle concentration (CMC) using a pyrene probe fluorescence method, as described below. The size (hydrodynamic diameter) and zeta potential of the PVA-Ppa nanoparticles were measured using dynamic light scattering (DLS) on a Microtrac instrument. The morphology of the nanoparticles was further examined by transmission electron microscopy (TEM) using a Philips CM-120 microscope operating at 200 kV.

2.3.4 Critical micelle concentration (CMC)

The critical micelle concentration (CMC) was determined by pyrene probe fluorescence using a ratiometric method. Serial

10.3389/fnano.2025.1690060

dilutions of PVA-Ppa (0.005–0.05 μM in PBS) were spiked with 1 μL of pyrene/acetone stock (0.1 mM) to achieve a final concentration of 0.1 μM . After a 2-h equilibration at 37 °C in 96-well black plates, fluorescence spectra were recorded with $\lambda_{ex} = 335$ nm and $\lambda_{em} = 372/383$ nm (I¹/I³ ratio). CMC values were determined from the inflection point of the sigmoidal curves.

2.4 Preparation and characterization of DOX-Loaded PVA-Ppa

2.4.1 Drug loading and nanoparticle preparation

Doxorubicin hydrochloride was converted to hydrophobic free base (DOX) through alkalization prior to loading. PVA-Ppa conjugates (20 mg) and DOX (1 mg) were co-dissolved in 2 mL anhydrous DMSO. The solution was adjusted to pH 8.5 with 0.1 M borate buffer and transferred into a dialysis bag (MW Cutoff = 3.5 kDa, Merck Millipore). Nanoparticle self-assembly was induced by dialysis against 1 L PBS (pH 7.4, 10 mM) at 25 °C for 3 h with buffer exchange every 30 min. The final nanoparticle dispersion was thus obtained in PBS at physiological pH 7.4.

2.4.2 Purification and determination of drug loading

Unencapsulated DOX was removed using centrifugal filters (MW Cutoff = 10 kDa, Merck Millipore) at 4,000×g for 15 min. Drug loading capacity and encapsulation efficiency were quantified via UV-Vis spectroscopy (Lambda 950, PerkinElmer). Briefly, 100 μL DOX-loaded PVA-Ppa-DOX were lysed with 900 μL DMSO, and absorbance at 480 nm was measured against a standard curve. The morphology of the DOX-loaded nanoparticles was examined using transmission electron microscopy (TEM). The hydrodynamic diameter and polydispersity index (PDI) were determined by dynamic light scattering (DLS).

2.4.3 *In vitro* drug release profile

The *in vitro* drug release kinetics were studied using a dialysis method. PVA-Ppa-DOX nanoparticles (2 mL, 1 mg/mL in PBS) were sealed in dialysis devices (MWCO = 3.5 kDa) and immersed in 1 L of PBS (pH 7.4) release medium containing 10 g/L activated charcoal to maintain sink conditions at 37 °C under continuous agitation (70 rpm). At predetermined time intervals, 1 mL aliquots of the release medium were withdrawn and replaced with an equal volume of fresh medium. The concentration of released DOX was quantified by measuring the absorbance at 480 nm.

2.5 Preparation and characterization of gadolinium-chelated PVA-Ppa

The metallation of PVA-Ppa conjugates was achieved through stoichiometric coordination with Gd³⁺ ions. The PVA-Ppa conjugate was first dissolved in a water/DMSO co-solvent system to dissociate any pre-assembled nanoparticles into molecularly dispersed polymer chains, thereby fully exposing the Ppa ligands for efficient chelation. This solution was then reacted with gadolinium (III) chloride (GdCl₃) at a 1:10 molar ratio (Ppa:

Gd3+) based on previous reports of porphyrin-Gd coordination chemistry (Zhdanova et al., 2023). The reaction mixture was stirred continuously at 80 °C for 3 days under nitrogen atmosphere to prevent oxidative degradation, conditions under which the covalent backbone of PVA-Ppa remains stable. Finally, the self-assembly of PVA-Ppa-Gd nanoparticles was induced by dialysis against deionized water. Unchelated Gd3+ ions were removed through sequential ultrafiltration using centrifugal devices (MW Cutoff = 10 kDa) with three cycles of concentration-dilution (4,000 × g, 15 min, 4 °C) in degassed PBS. The completeness of free ion removal was verified by Arsenazo III test (Hvattum et al., 1995). Briefly, a calibration curve was first established using standards of known Gd concentration. The purified nanoparticle solution was then tested with the Arsenazo III reagent. The absorbance of the reaction mixture is measured at the wavelength corresponding to the Gd-Arsenazo III complex using a UV-Vis spectrophotometer. The successful removal of free Gd was confirmed by the absence of the characteristic absorption peak at 660 nm, corresponding to the Gd3+-Arsenazo III complex. Final PVA-Ppa-Gd complexes were sterile-filtered (0.22 µm PVDF membrane). Morphological examination was conducted via TEM, while diameter and PDI were determined by DLS. Furthermore, the doxorubicin-loaded PVA-Ppa-Gd nanoparticles (PVA-Ppa-Gd-DOX) were prepared for the in vivo experiments. The drug loading procedure was identical to that used for PVA-Ppa-DOX (as described in Section 2.4.1), with the exception that the PVA-Ppa-Gd conjugate was used as the starting material instead of PVA-Ppa.

2.6 Stability testing

The colloidal stability of PVA-Ppa-DOX was investigated in different physiological media. Nanoparticle suspensions (1 mg DOX/20 mg PVA-Ppa) were dispersed in PBS and high-glucose culture medium (containing 10% fetal bovine serum), each aliquoted into 10 mL sterile vials (n = 3 per group). Samples were stored under room temperature with protection from light. At predetermined intervals (0, 12, 24, 36, 48, 60, 72 h, 144 h), 1 mL aliquots were withdrawn for particle size analysis. The particle size changes of nanoparticles in different environments over time were analyzed using DLS.

2.7 In vitro cell uptake and cytotoxicity

The uptake of PVA-Ppa nanoparticles in CNE-2 nasopharyngeal carcinoma cells were investigated through confocal microscopy. Cells were seeded and incubated with 50 μ g/mL PVA-Ppa (equivalent to 5 μ M Ppa) in serum-free medium for 0.5, 6, and 12 h. Post-incubation, cells underwent three PBS washes to arrest membrane trafficking, followed by fixation with 4% paraformaldehyde in PBS. Nuclei were counterstained with DAPI for 10 min. Confocal microscopy (LSM 880 with Airyscan, Zeiss) was performed using predefined acquisition parameter. Other cells were trypsinized and used for flow cytometry analysis. Cell viability was assessed using the MTS assay. Briefly, CNE-2 human nasopharyngeal carcinoma cells were seeded in 96-well plates and were exposed to free DOX, PVA-Ppa-DOX

(final concentration of DOX = $100~\mu M$), or empty PVA-Ppa nanoparticles. After 72 h incubation, MTS reagent was added per well and absorbance at 490 nm was measured using a microplate reader after 2 h incubation.

2.8 *In vitro* and *in vivo* photothermal irradiation

2.8.1 Assessment of photothermal conversion capability

The photothermal conversion efficiency of PVA-Ppa nanoparticles was quantitatively assessed *in vitro*. Nanoparticle suspensions were prepared in PBS at six predetermined concentrations (0, 0.02, 0.04, 0.08, 0.16, and 0.32 mg/mL, based on Ppa content), with some samples including sodium dodecyl sulfate (SDS) to simulate physiological surfactant exposure. The suspensions were irradiated using a calibrated 690 nm near-infrared laser system (Applied Optronics, Newport, CT) at a power density of 1 W/cm². The temperature changes were recorded in real-time using an infrared thermal camera (FLIR System).

2.8.2 *In vitro* photothermal therapy and mechanism study

For cellular studies, CNE-2 cells were pre-treated with empty PVA-Ppa nanoparticles (50 μg/mL) for 6 h. After washing thrice with PBS, the cells were irradiated with the 690 nm NIR laser (1 W/cm²) for 1-4 min. Cell viability was quantified 72 h post-irradiation using an MTS assay. To investigate the mechanism of photothermal therapy, intracellular reactive oxygen species (ROS) generation the fluorescent detected using probe 2',7'dichlorodihydrofluorescein diacetate (DCFH-DA). Following the respective treatments, cells were incubated with 10 µM DCFH-DA in serum-free medium at 37 °C for 30 min in the dark. After incubation, the cells were washed twice with PBS to remove excess probe. For fluorescence imaging, the cells were immediately observed using a Zeiss LSM 880 confocal microscope (excitation $\lambda = 488$ nm, emission $\lambda = 525$ nm). For quantitative analysis, the cells were trypsinized, resuspended in PBS, and analyzed immediately using a flow cytometer, measuring the fluorescence intensity of the oxidized DCF product in the FITC channel. Additionally, mitochondrial membrane potential was evaluated 18 h post-irradiation using the fluorescent probe 3,3-Dihexyloxacarbocyanine iodide (DiOC6(3)). Cells were co-stained with 50 nM DiOC6(3) and 1 µg/mL Propidium Iodide (PI) for 20 min at 37 °C, and fluorescence images were acquired using confocal microscope.

2.8.3 In vivo photothermal effect evaluation

The photothermal effect was assessed in BALB/c nude mice bearing CNE-2 nasopharyngeal carcinoma xenografts. Mice received an intravenous injection of PVA-Ppa nanoparticles (2 mg/kg Ppa equivalent in 100 μL PBS) via the tail vein. Twenty-four hours post-injection, the tumors were irradiated using the 690 nm diode laser system at a power density of 1 W/cm² for 180 s. Real-time thermographic monitoring was performed with a FLIR thermal camera. Control mice injected with PBS alone underwent the same irradiation procedure.

2.9 *In vitro* radiosensitization evaluation and apoptosis investigation

CNE-2 cells were plated into 96-well plates at a density of 5×10^3 cells per well, incubated at 37 °C with 5% CO₂ for 24 h. Subsequently, PBS, PVA-Ppa, and PVA-Ppa-Gd solutions (50 µg/mL) were introduced to the wells and co-incubated for an additional 2 h. PBS treatment served as a negative control. Unbound NPs were removed by washing with cold PBS, followed by exposure to 160 kVp X-ray irradiation (RS2000 irradiator, Rad Source Technologies) at doses of 0 (control), 2, 4, 6, or 8 Gy, and further incubation for 20 h. Cell viability and reactive oxygen species (ROS) production were subsequently assessed. For the colony formation assay, CNE-2 cells were treated with PBS, PVA-Ppa, and PVA-Ppa-Gd for 24 h. After removing excess nanoparticles, the cells were subjected to X-ray irradiation at doses of 0 (control), 2, 4, 6, and 8 Gy. Post-irradiation, cells were trypsinized and replated in 6-well plates at consistent densities. Cells were then incubated for 10 days. Colonies were stained with 0.4% crystal violet and counted, and the surviving fraction was determined by the ratio of colonies in irradiated wells to those in non-irradiated wells. The cell survival curve was modeled using a multitarget single-hit model (SF = $1-(1-e^{(-D/D0)})$), where SF represents the surviving fraction and D the radiation dose. The D₀ value was derived from the fitted curve. The sensitization enhancement ratio was calculated based on the radiation dose required to achieve 50% cell survival. For combination therapy studies, cells were pretreated with PVA-Ppa and PVA-Ppa-Gd (50 µg/mL) for 6 h followed by 4 Gy X-ray irradiation. After treatment, both adherent and floating cells were collected, washed twice with cold PBS, and resuspended in 1X Binding Buffer. The cell suspension was then stained with Annexin V-FITC and Propidium Iodide (PI) according to the manufacturer's instructions. The mixture was incubated for 15 min at room temperature in the dark. The stained cells were analyzed immediately using a flow cytometer. Data from 10,000 events were collected for each sample, and the percentage of cells in early apoptosis (Annexin V+/PI-) and late apoptosis (Annexin V+/PI+) was determined using FlowJo software (V 10.4).

2.10 Near-infrared fluorescence imaging

Tumor-bearing models (female BALB/c nude mice, 6–8 weeks, $18{\text -}22$ g) were established by subcutaneous injection of $5\times10^6\text{CNE-}2$ cells suspended in 100 μL PBS/Matrigel mixture (1:1 v/v) into the right flank. When tumors reached 6–10 mm in diameter, mice were randomized into experimental groups for imaging studies. For near-infrared fluorescence (NIRF) imaging, PVA-Ppa nanoparticles were administered via tail vein injection (20 mg/mL in 200 μL sterile PBS). Whole-body imaging was performed using the Kodak IS2000MM multimodal system at predetermined time points (15 min, 3, 6, 24, 48, 82 h) post-injection with the following parameters: 625 nm excitation/700 nm emission filters, 500 ms exposure time. Prior to imaging, mice were anesthetized with sodium pentobarbital. Tumors and all major organs were excised for $ex\ vivo$ imaging.

2.11 MRI imaging

T1 relaxivity measurements were performed on a Bruker BioSpec 7T/20 cm preclinical MRI system (Bruker Corporation) equipped with a 72 mm volume transceiver coil. Phantoms containing PVA-Ppa-Gd (0.125-1.0 mM Gd equivalent) and clinical contrast agent Gd-DTPA (Magnevist®, Bayer) as reference were scanned using a standardized FLASH (Fast Low Angle SHot) sequence: repetition rime (TR) = 200 ms, echo time (TE) = 4 ms, flip angle = 10° , field of view (FOV) = $60 \times 40 \text{ mm}^2$, $matrix = 128 \times 128$, slice thickness = 1.0 mm. Signal intensity (SI) was quantified using Paravision 6.0.1 software (Bruker) with regionof-interest (ROI) analysis covering 80% phantom area. T1 relaxation times were calculated via variable TR experiments. Nude mice bearing CNE-2 nasopharyngeal carcinoma xenograft were imaged on a Bruker Biospec 7T MRI scanner. To assess the kinetics of the PVA-Ppa-Gd in the body and tumour as well as the nanoparticleenhanced MRI signal intensity, a dynamic T1-weighted FLASH sequence (TR = 235.3 ms, TE = 4 ms, flip angle = 10° , FOV = $8 \times$ 6 cm (coronal) or 6×4 cm (axial), matrix size = 1.28×128 , and slice thickness = 1 mm) was used to acquire images just before injection and at predetermined time points post injection of PVA-Ppa-Gd (Gd dose: 0.015-0.02 mmol kg-1). A Multi-Slice Multi-Echo (MSME) sequence also employed for tumor imaging, with TR = 500 ms, TE = 15 ms, flip angle = 180° , FOV = 8×6 cm (coronal) or 6×4 cm (axial), matrix size = 128×128 , and slice thickness = 1 mm. MRI was also used to monitor the tumour changes in nude mice bearing CNE-2 nasopharyngeal carcinoma xenografts before and after radiotherapy, phototherapy and chemotherapy using the same parameters.

2.12 Evaluation of antitumor efficacy and combination therapy in xenograft mice

In vivo therapeutic studies were conducted using subcutaneous CNE-2 nasopharyngeal carcinoma xenograft-bearing mice. When tumor volumes reached 80-120 mm³ (designated Day 0), mice were randomized into nine groups (n = 5): (1) PBS, (2) free DOX (2.5 mg/kg), (3) PVA-Ppa-DOX (2.5 mg/kg DOX + 2 mg/kg Ppa), (4) PVA-Ppa + 1 W/cm² laser, (5) IR (X-ray irradiation, 160 kVp)+ PVA-Ppa, (6) IR + PVA-Ppa + 1 W/cm² laser, (7) IR + PVA-Ppa-Gd, (8) IR + PVA-Ppa-Gd + 1 W/cm² laser, and (9) IR + PVA-Ppa-Gd-DOX + 1 W/cm² laser. Treatments were administered every 5 days (Days 0, 5, 10, and 15) for four cycles. Following the injection of the nanoparticles, radiotherapy (RT, 2 Gy/fraction) and photothermal treatment (690 nm laser at 1 W/cm² for 120 s) were conducted 24 h later. Specifically, the PVA-Ppa and PVA-Ppa-Gd groups received radiotherapy only, and PVA-Ppa group received photothermal treatment only, while the PVA-Ppa, PVA-Ppa-Gd, and PVA-Ppa-Gd-DOX groups underwent combined therapy with RT and photothermal treatment (690 nm laser at 1 W/cm² for 120 s). Tumor volume (calculated as $[L \times W^2]/2$; L: longest diameter, W: shortest diameter) and body weight were monitored twice weekly. Mice were humanely euthanized when tumors exceeded 1,000 mm³. Blood samples collected 5 days post-treatment were analyzed for hematological and serum biochemical parameters. A single mouse from each cohort was euthanized, and the principal organs were excised for histopathological analysis.

2.13 Statistical analysis

Statistical evaluations were conducted utilizing the Student's t-test for pairwise group comparisons and the one-way ANOVA for analyses involving multiple groups. Data were consistently presented as mean ± standard deviation unless specified otherwise. A p-value of less than 0.05 was deemed indicative of statistical significance.

3 Results and discussion

3.1 Synthesis and characterization of PVA-Ppa nanoparticles

3.1.1 Chemical structure and synthesis verification

The PVA-Ppa conjugates were synthesized utilizing a covalent conjugation technique. Specifically, pyropheophorbide a, a chlorophyll-derived porphyrin analogue (Chen et al., 2009), was conjugated to the hydroxyl groups of PVA through a one-step esterification process. The detailed chemical structure and polymerization process were depicted in Figure 1A. The successful synthesis of PVA-Ppa was confirmed by the formation of stable polymeric structures. ¹H NMR spectra of PVA-Ppa revealed peaks that were unique for pyropheophorbide a (Figure 1B). The complex region between 0.8 and 3.0 ppm corresponded to the protons associated with pheophorbide a. Specific peaks in this region can be attributed to the various aliphatic and aromatic protons within the pheophytin molecule, including vinyl, ethyl, and methyl groups attached to the porphyrin ring system. These signals were crucial in confirming the presence and structural integrity of pheophorbide a within the composite. Then, the FTIR spectrum of the PVA-Ppa composite distinctly showed characteristic peaks of Ppa: out-of-plane C-H bending vibrations at ~3,390.86 cm⁻¹, conjugated porphyrin ring absorptions at 1,579.90 cm⁻¹ and 1,618.28 cm⁻¹, additional porphyrin ring bands at 987.55 cm⁻¹ and 1,095.57 cm⁻¹, alongside the PVA's free hydroxyl group stretching vibration at 1,095.57 cm⁻¹, indicating successful composite formation and interaction between PVA and Ppa (Figure 1C). The amount of conjugated porphyrin on PVA was calculated according to the calibration curve between the absorbance at 680 nm and concentrations of porphyrin standard (Supplementary Figure S1).

3.1.2 Physicochemical properties

The amphiphilic PVA-Ppa conjugates possessed the capability to self-assemble into micellar nanoparticles in aqueous solution, characterized by a hydrophobic porphyrin core encapsulated by hydrophilic PVA chains, facilitated by *in situ* π - π stacking interactions. TEM images demonstrated that these PVA-Ppa NPs exhibited a spherical morphology, accompanied by a relatively homogeneous size distribution around 35 nm (Figure 1D). DLS analysis indicated that the average diameter of PVA-Ppa NPs was (36.40 \pm 14.67) nm with a PDI of (0.18 \pm 0.06), which was consistent

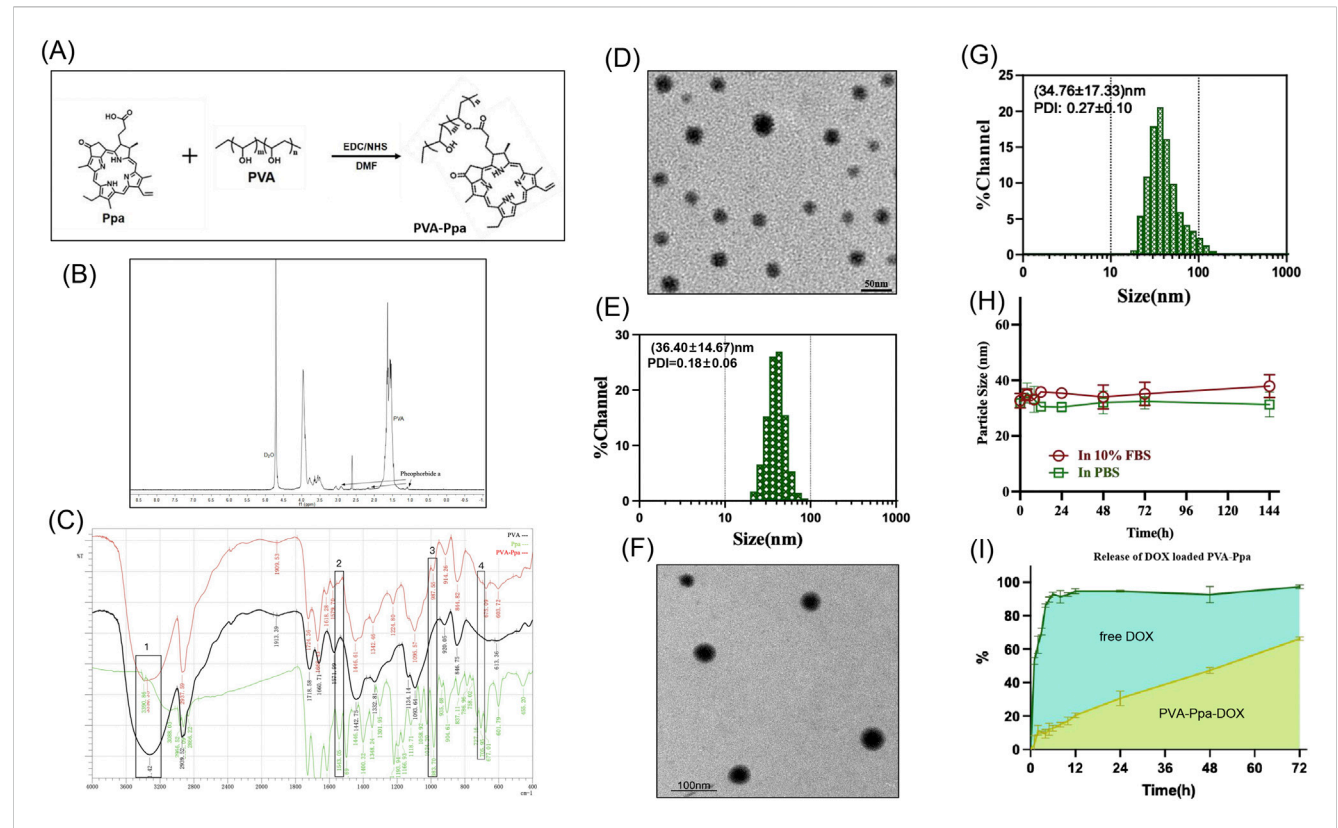
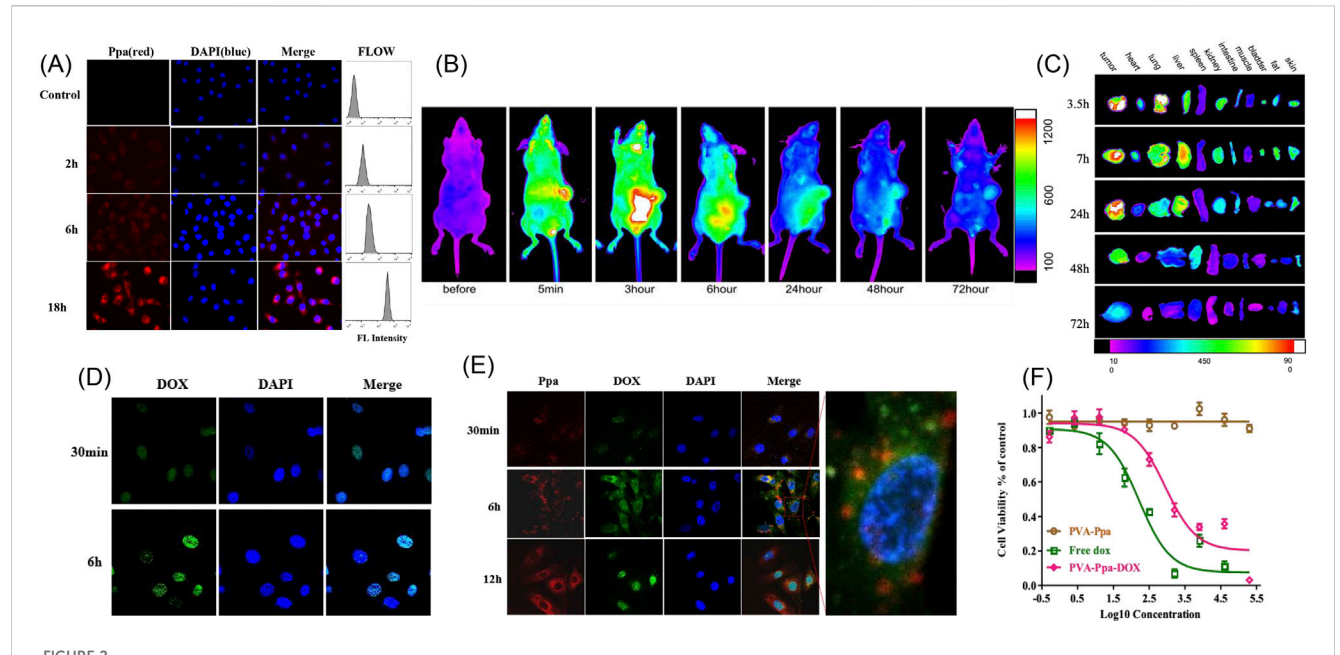


FIGURE 1 Synthesis, characterization, and drug release profile of PVA-Ppa nanoparticles. (A) Scheme of the synthesis of PVA-Ppa nanoparticles. (B) 1 H NMR spectra of PVA-Ppa conjugates in D₂O. (C) Fourier transform infrared spectroscopy (FTIR) spectrum of PVA-Ppa conjugates. 1 C-H, bending vibrations; 2 and 3, Characteristic absorption of the conjugated porphyrin ring; 4, Stretching vibrations of the free hydroxyl groups in PVA. (D) TEM image of PVA-Ppa nanoparticles. (E) Dynamic light scattering (DLS) analysis of PVA-Ppa nanoparticles. (F) TEM image of PVA-Ppa-DOX (1 mg DOX/20 mg PVA-Ppa). (G) DLS analysis of DOX-loaded PVA-Ppa nanoparticles (1 mg DOX/20 mg PVA-Ppa). (H) Particle size stability of PVA-Ppa-DOX over 144 h in PBS and 10% FBS. (I) In vitro drug release profile of PVA-Ppa-DOX and free DOX with dialysis method.

with that observed by TEM, suggesting a consistent and stable nanoparticle formulation (Figure 1E). Moreover, the zeta potential of the PVA-Ppa NPs was measured to be -18.5 mV (Supplementary Table S1). The presence of a negative surface charge in the aqueous medium indicated moderate colloidal stability. This stability enabled the NPs to repel each other to a certain extent via electrostatic interactions, thereby reducing aggregation tendencies and enhancing the dispersion stability of the aqueous system. The critical micelle concentration (CMC) of PVA-Ppa NPs, as determined through rigorous experimental procedures, was found to be 0.017 µM (Supplementary Figure value demonstrated a high efficiency and thermodynamic favorability for micelle formation at very low concentration levels. The fluorescent properties of PVA-Ppa were evaluated in PBS and SDS at various concentrations. The PVA-Ppa demonstrated two primary absorption peaks, specifically at 405 nm and within the near-infrared region at 680 nm (Supplementary Figure S3). In PBS, PVA-Ppa demonstrated subdued fluorescence, presumably attenuated due to π - π stacking interactions and the hydrophobic nature of porphyrin molecules. Upon exposure to SDS, which has the potential to destabilize the PVA-Ppa NPs, a marked enhancement in fluorescence intensity was detected (Supplementary Figure S4). Quantitative fluorescence analysis showed a marked enhancement in fluorescence intensity in SDS compared to PBS, with the highest fluorescence observed at 10 mg/mL concentration in SDS (Supplementary Figure S5). This fluorescence enhancement serves as direct evidence of SDS-induced disruption of the nanoparticle assembly (Mohammed et al., 2021; Lechuga et al., 2022). The disassembly liberates the Ppa molecules from their quenched state, confirming the structure's susceptibility to ionic surfactants. Thus, while the low CMC affirms a strong driving force for self-assembly, the fluorescence assay complements this by demonstrating the nanostructure's dynamic response to its environment.

3.1.3 Drug loading potential

The PVA-Ppa NPs were further evaluated for their drug delivery potential by loading them with DOX. TEM image revealed that the spherical morphology of these PVA-Ppa-DOX NPs (1 mg DOX/ 20 mg PVA-Ppa) resembled that of the unloaded PVA-Ppa NPs (Figure 1F; Supplementary Figure S6). DLS analysis of the DOX-loaded PVA-Ppa (PVA-Ppa-DOX) indicated an average particle size of (34.76 \pm 17.33) nm and a PDI of (0.27 \pm 0.10), which was comparable to the unloaded PVA-Ppa NPs, suggesting minimal size alteration upon drug loading (Figure 1G). However, the increase in PDI suggested that the incorporation of DOX introduced some degree of heterogeneity in the particle population. The loading efficiency (LE) for DOX approached 73% when the ratio of DOX



Cell uptake, *in vivo* and *ex vivo* near-infrared optical imaging of PVA-Ppa nanoparticles. (A) Cellular uptake of PVA-Ppa nanoparticles (0.1 mg/mL) in CNE-2 cells using laser confocal microscopy and flow cytometry (red, Ppa fluoresence; blue, DAPI for nucleus staining). (B) *In vivo* NIFR optical images (Ppa channel) of mice bearing CEN-2 xenografts at different time points post-administration of PVA-Ppa nanoparticles (5 mg/kg). (C) *Ex vivo* NIFR optical images (Ppa channel) of tumors and major organs of CNE-2 xenograft-bearing mice post-euthanization at different intervals. (D) Laser confocal images showing the internalization of free DOX (green fluoresence) in CNE-2 cells incubated with DOX (0.1 mg/mL) for 30 min and 6 h (blue, DAPI for nucleus staining). (E) Laser confocal images showing the uptake of PVA-Ppa-DOX in CNE-2 cells incubated with PVA-Ppa-DOX (0.1 mg/mL) for 30 min, 6 h and 12 h (red, Ppa fluoresence; green, DOX fluoresence; blue, DAPI for nucleus staining). (F) Cell viability curves comparing the cytotoxic effects of PVA-Ppa, free DOX, and PVA-Ppa-DOX on CNE-2 cells.

to PVA-Ppa NPs was 5% (w/w %) (Supplementary Figures S7, S8). The stability of PVA-Ppa-DOX was assessed in PBS and fetal bovine serum (FBS). The particle size remained relatively stable over 144 h, with no significant aggregation observed (Figure 1H). The *in vitro* release profile of free DOX and DOX encapsulated within PVA-Ppa NPs was investigated. As illustrated in Figure 1I, approximately 90% of the free DOX diffused into the buffer solution. In contrast, the release rate of DOX from PVA-Ppa-DOX NPs was lower, reaching less than 15% within the same time frame. Nevertheless, DOX continued to gradually diffuse from the PVA-Ppa-DOX NPs into the buffer, exhibiting a controlled and sustained release pattern. Over a 72-h period, the cumulative release of DOX from PVA-Ppa-DOX NPs reached 65%, compared to 97% for free DOX, indicating the potential of PVA-Ppa NPs for prolonged drug delivery applications (Figure 1I).

3.2 Cellular uptake and *in vivo* biodistribution study

3.2.1 In vitro cellular uptake and tumor targeting

The cellular uptake of PVA-Ppa NPs by CNE-2 cells was assessed using confocal laser scanning microscopy and quantified by flow cytometry (Figure 2A). A weak but detectable Ppa fluorescence was observed in CNE-2 cells after 2 h of incubation. The fluorescence signal showed a time-dependent increase, becoming more distinct at 6 h and reaching its maximum intensity at 18 h post-incubation. (Supplementary Figure S9). Flow cytometry analysis corroborated these findings, demonstrating a progressive increase in fluorescence

intensity in a time-dependent manner. These results suggested efficient internalization and accumulation of PVA-Ppa NPs within the CNE-2 cells. The in vivo biodistribution of PVA-Ppa NPs was evaluated in CNE-2 tumor-bearing mice using NIRF imaging (Figure 2B). Post administration, notable PVA-Ppa NPs accumulation was detected in the tumor region as early as 5 min, peaking at approximately 3 h postinjection. Substantial retention of PVA-Ppa NPS was observed until 72 h post-injection, indicating prolonged tumor targeting capability. Further examination of organ-specific accumulation involved ex vivo fluorescence imaging of harvested organs at various time points (Figure 2C). Tumor tissues exhibited the highest fluorescence intensity across all time points, confirming selective tumor targeting probably attributed to the enhanced permeability and retention (EPR) effect. Other organs, such as the liver and spleen, exhibited moderate accumulation, likely attributable to nonspecific phagocytic activity by Kupffer cells and macrophages (Asoudeh et al., 2024; Haroon et al., 2022). Additionally, a detectable fluorescence signal was observed in the lungs at the 3.5-h, 7-h and 24-h time points, but this signal decreased substantially at later time points (48 and 72 h). In other organs, including the heart, kidneys, intestine, muscle, blood, fat, and skin, only minimal fluorescence was observed across all time points. This overall profile, characterized by high and sustained tumor accumulation coupled with clearance from non-target organs like the lungs over time, signifies a favorable biodistribution and suggests reduced potential for long-term off-target effects.

3.2.2 Cytotoxicity and drug delivery advantages

Cellular uptake comparisons between free DOX and PVA-Ppa-DOX were conducted on CNE-2 cells. Confocal microscopy images

illustrated the localization and uptake dynamics. Figure 2D displayed increased green fluorescence in CNE-2 cells incubated with free DOX over 30 min and 6 h, indicative of DOX uptake and nuclear localization. After an incubation period of 6 h, the fluorescence signal of the free DOX was observed to be entirely localized within the nuclei (Supplementary Figure S10). In Figure 2E, CNE-2 cells, following treatment with PVA-Ppa-DOX, exhibited co-localization of red fluorescence (Ppa) and green fluorescence (DOX) across various incubation time points. Merged images affirmed the concurrent uptake and presence of both Ppa and DOX within the cells, demonstrating the effective targeted delivery of PVA-Ppa-DOX. In comparison to free DOX, the fluorescence intensity of DOX in the PVA-Ppa-DOX group was relatively low at 30 min but persisted at a high level within the cytoplasm at 6 h. Notably, at the 12-h time point, a significant portion of DOX had translocated into the cell nuclei, while Ppa remained predominantly in the cytoplasm (Supplementary Figure S11). Then, the cytotoxicity of PVA-Ppa, free DOX, and PVA-Ppa-DOX against CNE-2 cells was evaluated using MTS assays (Figure 2F). The viability data, presented as a function of concentration, revealed that free DOX exhibited a dose-dependent cytotoxic effect with significant cell viability reduction at higher concentrations. Comparatively, at the same DOX concentration and over the same time period, PVA-Ppa-DOX demonstrated a less cytotoxic effect due to its slower release of DOX. However, PVA-Ppa-DOX demonstrated sustained cytotoxicity with an enhanced effect when compared to free DOX over an extended period. The cytotoxicity of PVA-Ppa was minimal across all concentrations up to 20 mg/mL, thereby affirming its biocompatibility. This finding was consistent with the results obtained from previous studies, further validating the safety and applicability of PVA-Ppa in biomedical applications (Luo et al., 2017).

The observed cytoplasmic retention of DOX for up to 12 h, followed by gradual nuclear translocation, highlights controlled drug release as a key characteristic of our delivery system. This stands in contrast to the rapid nuclear uptake of free DOX. While the delayed nuclear accumulation may initially seem to be a limitation, as it correlates with the reduced immediate cytotoxicity at early time points, it is, in fact, a strategically designed feature. This temporal control offers significant advantages. First, the extended cytoplasmic residence time may help circumvent drug resistance mechanisms, such as P-glycoprotein efflux, which often target drugs in the cytoplasm before they reach the nucleus (Shi et al., 2024; Hammond et al., 2025). Second, the sustained release ensures a prolonged therapeutic pressure on cancer cells, which is critical for effective tumor suppression, as evidenced by the potent cytotoxicity observed over longer incubation periods (Guerassimoff et al., 2024). Finally, this mechanism is likely to contribute to a improved safety profile. By minimizing the amount of freely diffusible DOX during circulation, the nanoparticle formulation reduces the risk of off-target toxicity to healthy tissues. Therefore, the delayed action is a trade-off for enhanced specificity and sustained efficacy.

3.3 PVA-Ppa-Gd NPs-mediated MR imaging

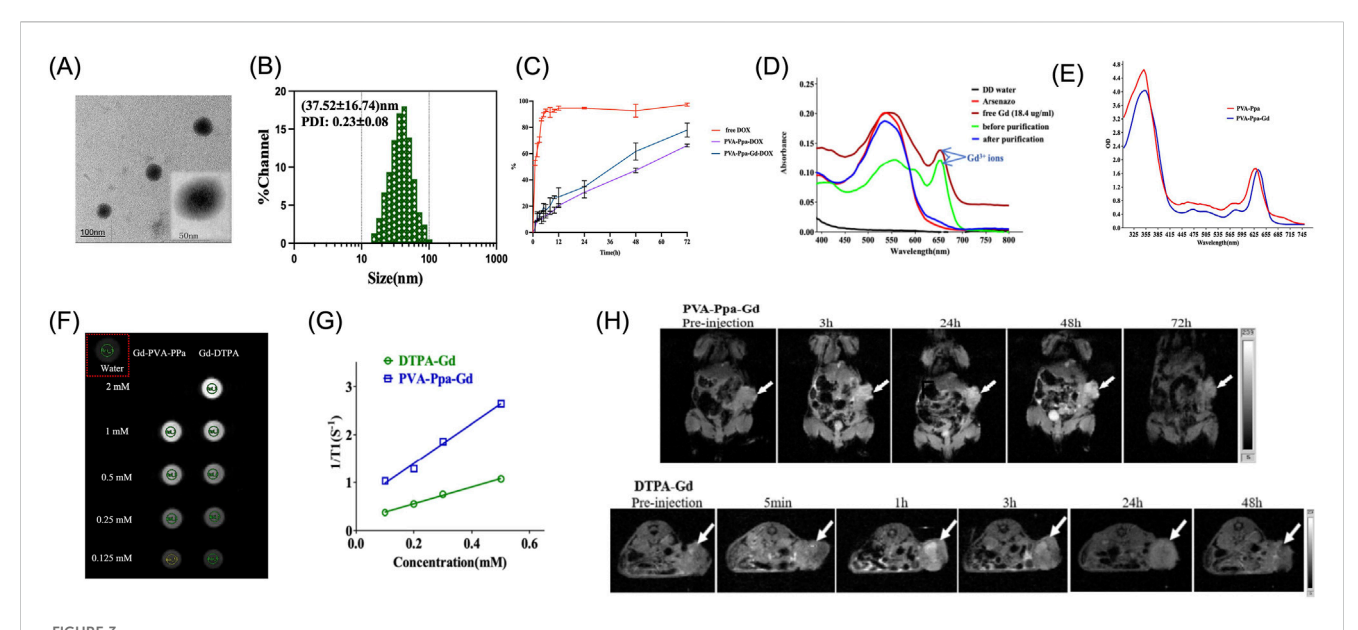
3.3.1 Nanoparticle characterization and drug loading properties

Reports indicate that porphyrins and their tetrapyrrole-based derivatives exhibit the capability to coordinate with a remarkably

wide variety of metal ions, resulting in the formation of metalloporphyrin complexes (Alpatova et al., 2025; Boonyuen et al., 2024; Martynov et al., 2022). Leveraging the intrinsic properties of these coordinated metal ions, they can serve as contrast agents in imaging applications (Jin et al., 2022; Martynov et al., 2022). In this study, gadolinium (Gd³⁺), known for its efficacy as a T1-weighted MRI contrast agent, was employed to chelate with porphyrin. The morphology and size of the synthesized PVA-Ppa-Gd NPs were examined using TEM, as shown in Figure 3A (Supplementary Figures S12, S13). The TEM image revealed uniform spherical structures without noticeable aggregation. The size distribution and PDI of the PVA-Ppa-Gd NPs, as measured using DLS and displayed in Figure 3B, were determined to have an average hydrodynamic diameter of (37.52 ± 16.74) nm with a PDI of (0.22 \pm 0.08), indicating a relatively narrow size distribution. When compared to empty PVA-Ppa NPs, the PVA-Ppa-Gd NPs exhibited a relatively broader size distribution and larger average hydrodynamic diameter (Supplementary Table S1). This difference in size distribution and PDI was likely due to the incorporation of Gd ions into the PVA-Ppa matrix, which may have influenced the self-assembly process and resulted in a broader size distribution. Based on the successful formation of PVA-Ppa-Gd NPs, DOX loading capacity was further evaluated. The result showed a slight but measurable decrease in loading capacity compared to the non-chelated PVA-Ppa-DOX NPs, attributing to Gd3+-induced modifications in the self-assembled structure. As supported by increased hydrodynamic size and polydispersity (Figure 3B), the nanoparticle core appears less densely packed, resulting in fewer hydrophobic domains available for DOX incorporation. We then examined the DOX release profile from PVA-Ppa-Gd-DOX NPs. While the formulation maintained a sustained release pattern, its kinetics differed from PVA-Ppa-DOX. Notably, an enhanced initial burst release was observed, with approximately 25% of DOX released within the first 12 h, compared to about 15% for the PVA-Ppa-DOX NPs (Figure 3C). This accelerated release rate is consistent with the observed physicochemical changes. Over the extended 72-h period, the cumulative release from PVA-Ppa-Gd-DOX reached approximately 75%, which is slightly higher than the 65% observed for PVA-Ppa-DOX. This further supports the notion of a structurally modified, somewhat less stable nanoparticle assembly. Crucially, despite these kinetic differences, the Gd-chelated platform maintained a fundamentally controlled and sustained release profile, confirming its retained functionality as a drug carrier while endowing the system with additional capabilities for MRI and radiosensitization.

3.3.2 MR imaging and in vivo application

After Gd chelation, the absorption spectrum of PVA-Ppa-Gd exhibited a 5-nm red-shift (Figure 3D). This red-shift suggested a change in the electronic structure of the PVA-Ppa upon Gd ion chelation, potentially enhancing its relaxation properties for MRI applications. The residual Gd^{3+} content following purification was evaluated using the Arsenazo III test (Supplementary Figures S14), with results depicted in Figure 3E. The spectrum compared deionized water (DD water), Arsenazo III reagent, free Gd^{3+} (18.4 μ g/mL), and samples before and after purification. The post-purification spectrum closely aligned with the baseline,



Characterization of Gd³⁺ chelated PVA-Ppa and MR imaging properties. (A) TEM image of PVA-Ppa-Gd nanoparticles. (B) Dynamic light scattering (DLS) analysis of PVA-Ppa-Gd nanoparticles. (C) *In vitro* drug release profile of PVA-Ppa-Gd-DOX with dialysis method. PVA-Ppa-DOX and free DOX were used as controls. (D) The absorption spectra of blank PVA-Ppa (red) and PVA-Ppa-Gd (blue). (E) Absorption spectra of Arsenazo III solution with PVA-Ppa-Gd solution after centrifuge filtration. (F) *In vitro* MRI signal of PVA-Ppa-Gd and DTPA-Gd obtained by T1-weighted MRI on a Bruker Biospec 7T MRI scanner using a FLASH sequence. (G) T1 relaxivity coefficient of PVA-Ppa-Gd NPs and DTPA-Gd. (H) *In vivo* MR imaging of PVA-Ppa-Gd and DTPA-Gd on CNE-2 tumor-bearing mice using Bruker Biospec 7T MRI with FLASH sequence. The white arrow indicates the tumor.

indicating effective removal of unbound Gd³⁺ from the nanoparticle solution. The T1 contrast capability of PVA-Ppa-Gd NPs was evaluated at 7 T field strengths and compared with Gd-DTPA, a clinically utilized contrast agent (Figure 3F). The relaxation rates serve as pivotal parameters in MRI, significantly influencing image contrast and signal intensity, and consequently, the diagnostic efficacy of MRI scans (Zhang et al., 2024; Daniel et al., 2023). At a field strength of 7 T, the PVA-Ppa-Gd NPs exhibited superior contrast performance, demonstrating a notably higher T1 relaxivity (r1) value (4.17 mM⁻¹.s⁻¹) when compared to Gd-DTPA) (1.76 mM⁻¹.s⁻¹) (Figure 3G).

In this study, a T1-weighted FLASH sequence was utilized, characterized by specific parameters: TR = 235.3 ms, TE = 4 ms, and a flip angle of 10°. This configuration resulted in a decreased r1 value for DTPA-Gd, which was lower than the typical value (~4 mM⁻¹.s⁻¹) observed under standard field strengths of 1.5T or 3T (Zhang et al., 2023; Liu et al., 2025). At 7T, the observed decrease in r1 for DTPA-Gd was likely attributed to a confluence of high-field effects and incomplete T1 recovery stemming from the employed short TR (Gkotsis et al., 2025; Zhang et al., 2024). Conversely, the r1 value of PVA-Ppa-Gd NPs was measured at 4.17 mM⁻¹.s⁻¹, clearly demonstrating their robust T1 contrast efficacy at 7T. The high r1 value was a clear indication of the efficient interplay between the nanoparticles and water molecules, facilitating accelerated longitudinal relaxation and enhanced image contrast (Wang et al., 2024). Notably, the adoption of FLASH sequence with short TR and TE values aimed to establish an equilibrium between achieving effective T1 enhancement and minimizing scan duration a significant consideration given that traditional MRI scans often necessitate prolonged scanning times, posing notable constraints in clinical and research settings (Priovoulos et al., 2023). In vivo MR imaging experiments were conducted to evaluate the contrast enhancement in CNE-2 tumor-bearing mice using PVA-Ppa-Gd NPs and DTPA-Gd (Figure 3H). The PVA-Ppa-Gd NPs group exhibited significant signal enhancement at the tumor at various time points, with the peak signal observed at 48 h post-injection. In contrast, the DTPA-Gd group demonstrated a rapid decline in signal intensity at the tumor site over time, with a notable signal at 5 min post-injection and a substantial reduction at 3 h. This underscores the prolonged and stable contrast enhancement provided by PVA-Ppa-Gd NPs *in vivo*.

3.4 Photothermal effect of PVA-Ppa NPs

3.4.1 Photothermal conversion efficiency *in vitro* and *in vivo*

In the context of photothermal therapy, the fluorescence characteristics of nanoparticles play a crucial role in understanding their behavior and efficiency in biological environments. Figure 4A demonstrated the fluorescence imaging of PVA-Ppa NPs in SDS and PBS. As PVA-Ppa NPs were highly self-quenched in PBS, the thermal effect of PVA-Ppa NPs was evaluated using a thermal camera. The temperature increased rapidly from 29.6 °C to 54.4 °C when PVA-Ppa in PBS solutions at a concentration of 0-0.32 mg/mL were exposed to 690 nm laser at 1 W/cm² for 30 s, which was significantly higher than that in SDS solutions (P < 0.05) (Figure 4B). The *in vivo* photothermal conversion efficiency of PVA-Ppa NPs was further assessed by monitoring tumor temperature during irradiation with 690 nm laser at 1 W/cm², in comparison to PBS control groups (Figures 4C-E). The temperature changes after irradiation in CNE-2 tumorbearing mice 24 h post-injection with PVA-Ppa (5 mg/kg) versus PBS were recorded. Figure 4F presented a quantitative analysis of 10.3389/fnano.2025.1690060

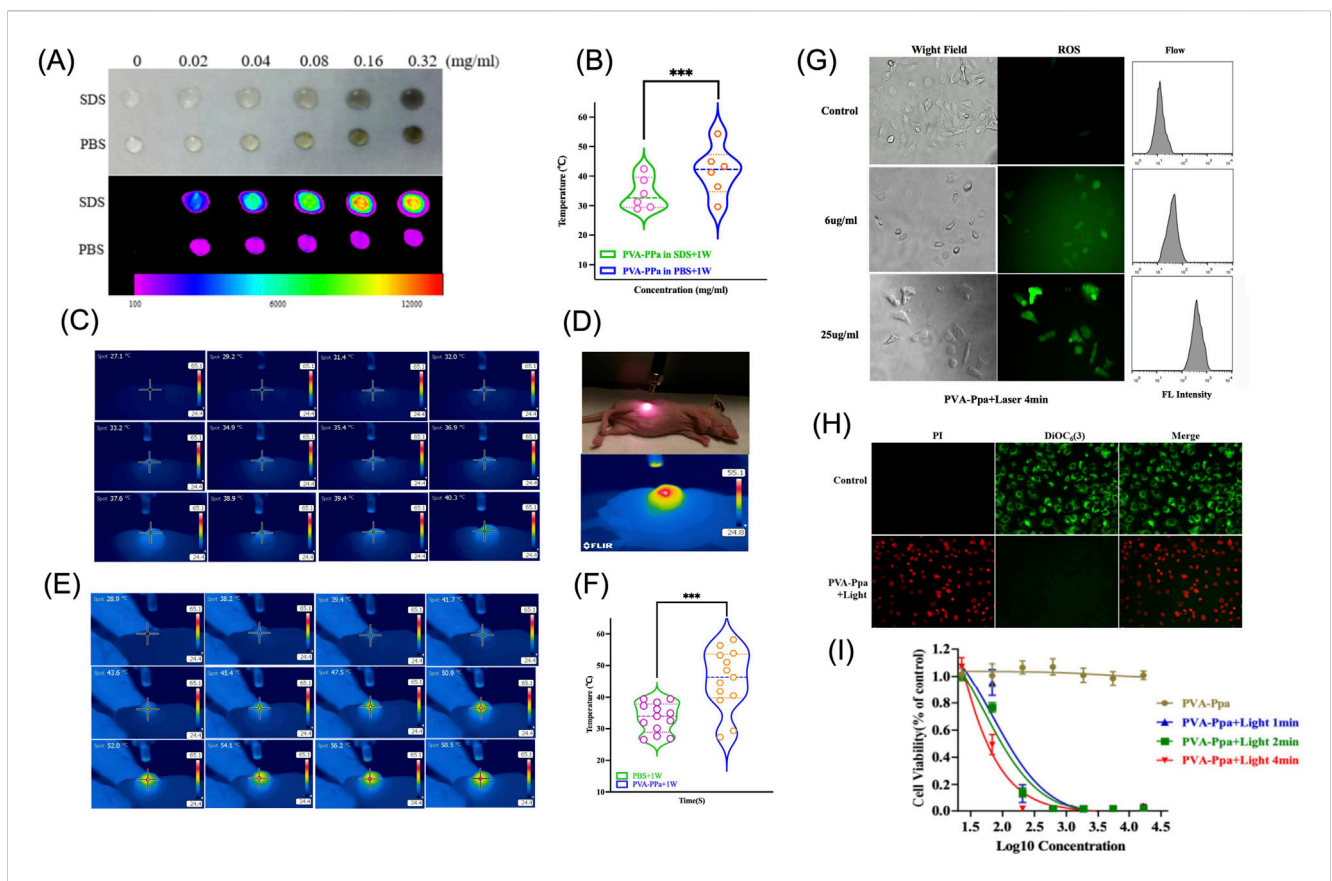


FIGURE 4
Photothermal Effect of PVA-Ppa nanoparticles. (A) NIFR fluorescence imaging of PVA-Ppa NPs in the presence and absence of SDS, using an excitation filter at 625 nm and an emission filter at 700 nm. (B) Temperature variations assessed using a thermal imaging camera with PVA-Ppa in SDS and PBS. (C) Thermal imaging of CNE-2 tumor-bearing mice injected with PBS. (D) Representation of the laser irradiation setup with CNE-2 tumor-bearing mice. (E) Thermal imaging of CNE-2 tumor-bearing mice injected with PVA-Ppa. (F) Temperature variations assessed using a thermal imaging camera on CNE-2 tumor-bearing mice post-injection of PVA-Ppa and PBS. (G) The generation of ROS in CNE-2 cells treated with varying concentrations of PVA-Ppa and subjected to a 1-min light exposure. Cells were stained with 10 μM dichlorodihydrofluorescein diacetate (DCFH-DA) (green fluorescence). (H) The effect of PVA-Ppa induced mitochondrial depolarization in CNE-2 cells visualized using confocal imaging. Cells were stained with 50 nM DiOC₆(3) (green, mitochondrial membrane potential), and propridium iodide (red, dead cells). (I) Cell viability of CNE-2 cells treated with different concentrations of PVA-Ppa and light exposure at various durations (1, 2, and 4 min).

temperature changes across different time points. Specifically, the temperature of the PVA-Ppa NPs group exhibited a rise from 27.3 °C to 58.2 °C over a period from 0 to 240 s. In contrast, PBS group showed a comparatively lower temperature increase from 26.5 °C to 39.4 °C within the same time frame. Statistical analysis using Student's t-test confirmed the significant difference (P < 0.01) between the two groups, with a marked increase in temperature observed in the PVA-Ppa NPs group, indicating effective photothermal conversion.

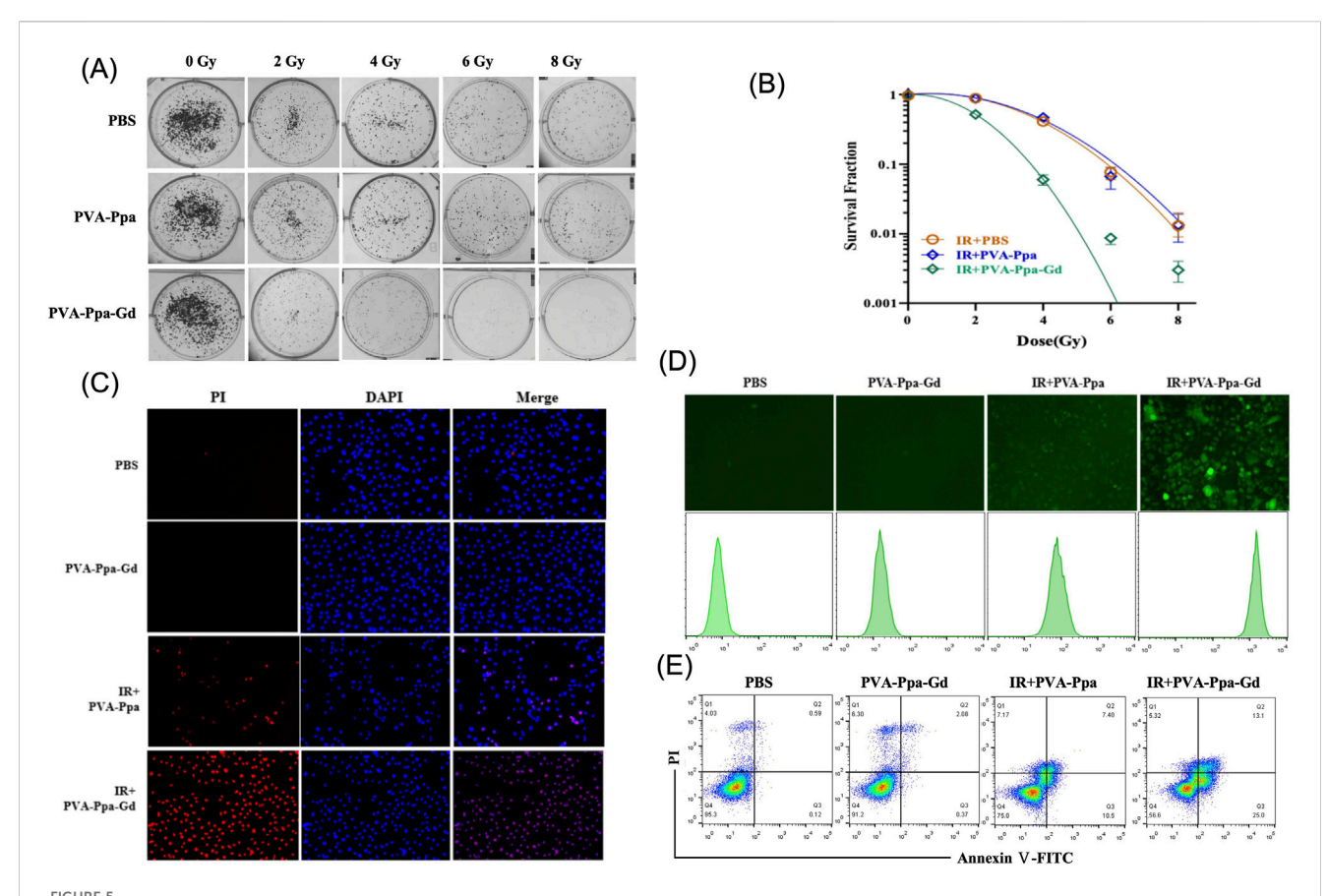
3.4.2 Mechanisms of photothermal-induced cell death

The mechanism of cell death after light irradiation was further investigated. Figure 4G investigated ROS generation in CNE-2 cells exposed to different concentrations of PVA-Ppa NPs under laser irradiation (Supplementary Figure S15). Confocal images revealed a significant rise in ROS levels in a dose-dependent manner, confirmed by flow cytometry results, indicating enhanced oxidative stress inflicted by PVA-Ppa NPs upon light activation. To further investigate the mechanism of cell death induced by PVA-Ppa, Figure 4H illustrated the mitochondrial depolarization by propidium iodide (PI) and 3,3'-Dihexyloxacarbocyanine Iodide (DIOC₆(3)) co-staining in CNE-2 cells

exposed to PVA-Ppa and laser irradiation (Supplementary Figure S16). Cells in the control group displayed green fluorescence of DIOC₆(3) without red fluorescence of PI, whereas cells in the treated group displayed only red fluorescence of PI, suggesting that the cells were killed upon laser irradiation. Finally, the phototoxic effect of PVA-Ppa NPs against CNE-2 cells was studied, by exposure of NIR light at 1 W/ cm² for 1 min, 2 min and 4 min, respectively (Figure 4I). The results showed a significant decrease in cell viability with increasing exposure time, demonstrating the potent cytotoxic effect of PVA-Ppa NPs under laser irradiation.

3.5 PVA-Ppa-Gd NPs-mediated radiosensitization

High-Z metals such as gold (Au) and gadolinium (Gd) have been extensively explored as radiosensitizers in radiotherapy due to their ability to enhance radiation dose deposition and improve therapeutic efficacy (Chargari et al., 2024; Moloudi et al., 2023). To evaluate the radiosensitization effect of PVA-Ppa-Gd NPs on CNE-2 nasopharyngeal carcinoma cells, a clonogenic survival assay



PVA-Ppa-Gd NPs-mediated radiosensitization. (A) Clonogenic survival assay on CNE-2 cells treated with PBS, PVA-Ppa, or PVA-Ppa-Gd, followed by exposure to varying doses of radiation (0, 2, 4, 6, and 8 Gy). (B) Survival fractions of PBS, PVA-Ppa, and PVA-Ppa-Gd under various radiation doses. (C) Fluorescence microscopy showed enhanced cell death in PVA-Ppa-Gd group following 4 Gy X-ray irradiation. Cells were stained with propridium iodide (red, dead cells) and DAPI (blue, nuclei). (D) Confocal microscopy and flow cytometry demonstrated enhanced ROS generation in PVA-Ppa-Gd group following 4 Gy X-ray irradiation. Cells were stained with 10 μM dichlorodihydrofluorescein diacetate (DCFH-DA) (green fluorescence). (E) Flow cytometry of Annexin V/PI revealed increasing of cell apoptosis in PVA-Ppa-Gd group following 4 Gy X-ray irradiation.

was performed (Figure 5A). The cells were treated with PBS, PVA-Ppa, or PVA-Ppa-Gd, followed by exposure to varying doses of X-ray radiation (0, 2, 4, 6, and 8 Gy). The PBS-treated cells maintained notable clonogenicity across all radiation doses. Similarly, cells treated with PVA-Ppa NPs did not exhibit a significant dosedependent reduction in colony formation. Conversely, cells treated with PVA-Ppa-Gd NPs exhibited significant reduction in clonogenic survival across all dosages, particularly at higher radiation doses. The clonogenic cell survival assay was performed to verify if PVA-Ppa-Gd NPds increased radiation sensitivity. By fitting a multitarget single-hit model to the cell survival curve, the sensitization enhancement ratio (SER) of PVA-Ppa-Gd NPs was calculated to be 1.69 (Figure 5B). This indicated that the accumulation of PVA-Ppa-Gd in the cells markedly boosted radiation sensitivity. These findings were consistent with the hypothesis that the combination of PVA-Ppa-Gd NPs and radiation therapy synergistically enhanced cell death in target cells. Further, fluorescence microscopy visualized cell death induced by X-ray irradiation (Figure 5C; Supplementary Figure S17). Minimal cell death was observed in the PBS and PVA-Ppa-Gd groups without irradiation, but significant cell apoptosis was seen in the irradiation group, especially in the PVA-Ppa-Gd group. Additionally, pathological analysis showed extensive cellular disruption and increased apoptosis compared to the control and Pva-Ppa groups (Supplementary Figure S18). X-ray irradiation induced secondary damage mainly through ROS generation. Confocal microscopy and flow cytometry assessed ROS levels post-irradiation, showing a marked increase in ROS production in cells treated with PVA-Ppa-Gd upon exposure to 4 Gy X-ray irradiation (Figure 5D; Supplementary Figure S19). The augmented ROS generation in the PVA-Ppa-Gd group was attributed to the radiosensitizing properties of the nanoparticles. Finally, Annexin V/PI flow cytometry analysis examined the apoptotic response in CNE-2 cells treated with PVA-Ppa-Gd NPs and exposed to 4 Gy X-ray irradiation. The data revealed a substantial increase in apoptotic cells in the PVA-Ppa-Gd group, with apoptosis rates reaching approximately 40%, compared to 17% in the PVA-Ppa group, highlighting the significant radiosensitizing effect of PVA-Ppa-Gd NPs (Figure 5E).

3.6 Anti-tumor efficacy of PVA-Ppa-Gd NPsmediated multimodal therapy and MRIguided therapy

3.6.1 *In Vitro* cytotoxicity and synergistic mechanisms

The in vitro cytotoxic effects of free DOX, PVA-Ppa-DOX, PVA-Ppa+1 W/cm^2 (690 nm laser, 30 s), IR (160 kVp X-ray

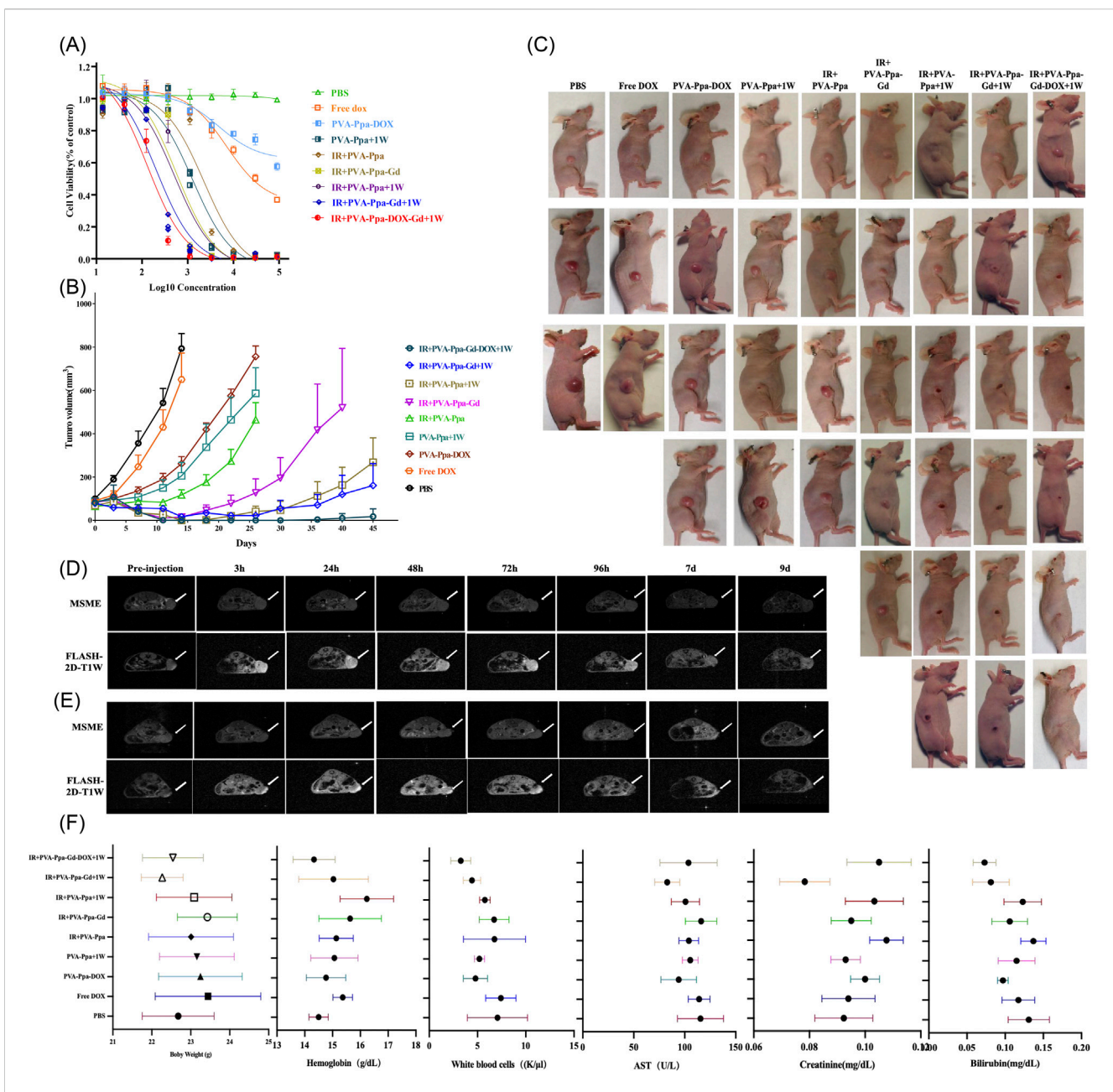


FIGURE 6
Anti-tumor efficacy of PVA-Ppa NPs-mediated multimodal therapy. (A) In vitro cytotoxic effects of PVA-Ppa formulations mediated chemotherapy, photothermal therapy, radiotherapy or their combination therapy on CNE-2 cells. (B) In vivo antitumor efficacy after the intravenous administration of various DOX formulations combined with PVA-Ppa mediated photo-therapy, or radiotherapy (n = 5). The CNE-2 tumor-bearing mice were intravenously injected with PBS (control), free DOX (2.5 mg/kg), PVA-Ppa formulations (2 mg/kg calculate on porphyrin) on day 0, 5, 10 and 15 followed by X-ray or laser irradiations on tumors at 24 h post injection. (C) Representative photographs showing therapeutic response to PVA-Ppa mediated chemotherapy, radiotherapy, or photothermal therapy, respectively. (D) Longitudinal MRI imaging (axial) of untreated CNE-2 tumor bearing mice. (E) Longitudinal MRI imaging (axial) of tumor regression in treated CNE-2 tumor bearing mice. Arrows indicate tumor. (F) Body weight, blood cell counts and serum chemistry changes of mice receiving various regimens of treatment.

irradiation, 4 Gy) + PVA-Ppa, IR + PVA-Ppa-Gd, IR + PVA-Ppa+1 W, and the combination therapy (IR + PVA-Ppa-Gd+1 W and IR + PVA-Ppa-Gd-DOX+1W) on CNE-2 cells were assessed using an MTS assay (Figure 6A). Free DOX exhibited rapid, dose-dependent cytotoxicity, consistent with its fast cellular uptake. In contrast, PVA-Ppa-DOX showed a distinct profile. While its cytotoxicity was initially lower at early time points, likely due to the time-dependent release of DOX from the nanocarrier, it

demonstrated significant and sustained toxicity at higher concentrations and longer incubations. This confirms that the nanoparticle formulation provides controlled drug release. The superior efficacy of the triple-combination therapy (IR + PVA-Ppa-Gd-DOX + Laser) is attributed to a synergistic interaction between the modalities. PTT induced by the laser not only causes direct hyperthermia-mediated cell damage but also enhances tumor vascular permeability and blood flow, potentially improving

nanoparticle delivery and promoting the release of encapsulated DOX. Simultaneously, the presence of Gd in the nanoparticles acts as a radiosensitizer, enhancing the lethal damage from X-ray irradiation. When combined with the chemotherapeutic effect of the released DOX, this multi-faceted attack results in significantly greater cell death compared to any mono- or dual-therapy.

3.6.2 *In Vivo* antitumor efficacy and MRI-guided therapy monitoring

The anti-tumor efficacy of PVA-Ppa-Gd NPs was further investigated using an in vivo subcutaneous tumor model bearing CNE-2 xenografts. Mice were treated intravenously with free DOX, PVA-Ppa-DOX and PVA-Ppa-Gd-DOX at equivalent DOX doses (2.5 mg/kg), all PVA-Ppa formulations at equivalent porphyrin doses (2 mg/kg), in addition to a PBS control, every 5 days on days 0, 5, 10, and 15. The data showed that mice treated with 2.5 mg/kg PVA-Ppa + DOX demonstrated marked tumor growth suppression compared to the free DOX group. Tumors treated with PVA-Ppa-Gd and X-ray irradiation (160 kVp, 2 Gy/fraction) also demonstrated reduced growth rates. Interestingly, the combination treatment with X-ray irradiation and laser irradiation resulted in significantly delayed tumor growth compared to either treatment alone. Notably, the combination therapy of PVA-Ppa-Gd + DOX with both X-ray and laser irradiation achieved 100% survival rate since three cycles treatment. By day 45, only one out of five mice received this combination therapy exhibited tumor recurrence (Figures 6B,C). Further, pathological examination suggested that the combined treatment induced more severe cellular damage compared to photothermal therapy alone (Supplementary Figure S20). To achieve image-guided precision treatment and efficacy monitoring during therapy, we conducted a longitudinal assessment of CNE-2 tumor-bearing mice models using two MRI sequences: Multi-Slice Multi-Echo (MSME) and Fast Low Angle Shot (FLASH). Figure 6D illustrated the progression of tumors in untreated mice, with imaging conducted at multiple intervals. The images revealed significant signal enhancement at various time points, with the highest signal observed between 48-72 h. In contrast, Figure 6E depicted imaging from mice receiving therapeutic intervention, displaying the dynamic regression of tumors over the same time points. The MSME and FLASH-2D-T1W sequences offered critical insights, with MSME providing highresolution images for tumor delineation and FLASH enhancing structural details (Supplementary Figure S21). Throughout the monitored period, the imaging sequences exposed significant morphological and signal intensity changes indicative of tumor regression in the treated group. These findings highlighted the utility of MRI-guided monitoring in evaluating therapeutic efficacy, demonstrating the potential for real-time assessment of tumor response to treatment. This imaging approach can guide clinical decisions and optimize therapeutic strategies by offering detailed temporal and spatial data on tumor dynamics.

3.6.3 Biosafety and biocompatibility assessment

The biosafety profile of PVA-Ppa and the related formulations was systematically investigated in all treated mice. Longitudinal tracking of body weight variations demonstrated comparable growth patterns across all treatment groups relative to PBS controls, with no significant weight reduction observed during the therapeutic regimen (Figure 6F). Hematological analysis conducted

5 days post-final administration (Day 15) revealed maintained peripheral blood cell counts, including RBC, HBG, and PLT showing no statistically meaningful deviations from baseline control values (PBS group). The WBC of the mice receiving combined treatment (both X-ray and laser irradiation) showed a certain degree of decline, but it was still within a reasonable range. Serum biochemistry parameters associated with hepatic function (ALT, AST) and renal clearance (BUN, creatinine) remained within normative physiological ranges across all treatment cohorts. A slight elevation in total bilirubin levels was transiently detected in the combination therapy group following X-ray irradiation (Figure 6F). Terminal histopathological examination of major organs (heart, liver, spleen, lungs, kidneys) harvested at the experimental endpoint (day 50) confirmed preserved tissue integrity without evidence of treatment-induced pathological alterations (Supplementary Figure S21). These cumulative findings substantiate the favorable biocompatibility of the developed formulations under the described experimental conditions.

4 Conclusions and future perspectives

This study successfully developed a versatile PVA-Ppa-Gd nanotheranostic platform for precise MRI-guided combinatorial therapy. The well-characterized nanoparticles exhibited excellent stability, efficient drug loading, and tumor-targeted accumulation via the EPR effect. PVA-Ppa-Gd served as a highly effective T1 contrast agent (r1 = $4.17 \text{ mM}^{-1}.\text{s}^{-1}$ at 7T), enabling prolonged and precise tumor Furthermore, PVA-Ppa demonstrated photothermal conversion, while PVA-Ppa-Gd acted as a significant radiosensitizer (SER = 1.69), enhancing radiation-induced ROS generation and apoptosis. Critically, the triple-modality therapy combining MRI-guided photothermal therapy, chemotherapy, and radiotherapy achieved synergistic efficacy, resulting in complete tumor regression and 100% survival in vivo with minimal systemic toxicity. While the current findings provide a robust proof-of-concept for the platform's design and potent antitumor activity, we acknowledge that the subcutaneous model does not fully replicate the anatomical complexity of nasopharyngeal carcinoma. Therefore, these highly promising results strongly justify and form the foundation for future studies employing more clinically relevant orthotopic models. This integrated nanoplatform represents a compelling strategy for precision theranostics, with its full potential awaiting further validation in advanced disease settings.

Data availability statement

The original contributions presented in the study are included in the article/Supplementary Material, further inquiries can be directed to the corresponding author.

Ethics statement

The animal study was approved by the Animal Ethics Committee of Chongqing University Cancer Hospital. The study was conducted in accordance with the local legislation and institutional requirements.

Author contributions

X-YL: Conceptualization, Methodology, Writing – original draft. Y-NY: Methodology, Writing – original draft, Formal Analysis. YX: Writing – original draft, Data curation, Resources. LH: Data curation, Resources, Writing – original draft. Y-YL: Writing – original draft, Investigation, Validation. QL: Investigation, Validation, Writing – original draft. CW: Investigation, Writing – original draft. YL: Conceptualization, Funding acquisition, Methodology, Visualization, Writing – review and editing.

Funding

The author(s) declare that financial support was received for the research and/or publication of this article. This research was supported by the National Natural Science Foundation of China (No. 82272755), Chongqing Science and Technology Commission (No. 2022NSCQ-MSX0706), and Fundamental Research Funds for the Central Universities (No. 2022CDJYGRH-007).

Conflict of interest

The authors declare that the research was conducted in the absence of any commercial or financial relationships that could be construed as a potential conflict of interest.

References

Alpatova, V. M., Nguyen, M. T., Rys, E. G., Liklikadze, G. K., Kononova, E. G., Smol'yakov, A. F., et al. (2025). Metal (M = Cr, Mo, W, Re) carbonyl complexes with porphyrin and carborane isocyanide ligands: light-induced oxidation and carbon oxide release for antitumor efficacy. *Biomater. Sci.* 13 (3), 711–730. doi:10.1039/d4bm01293c

Alsavaf, M. B., Marquardt, M., Abouammo, M. D., Xu, M., Elguindy, A., Grecula, J., et al. (2025). Patient characteristics and treatment outcomes of nasopharyngeal carcinoma in nonendemic regions. *JAMA Netw. Open* 8 (3), e251895. doi:10.1001/jamanetworkopen.2025.1895

Asoudeh, M., Nguyen, N., Raith, M., Denman, D. S., Anozie, U. C., Mokhtarnejad, M., et al. (2024). PEGylated nanoparticles interact with macrophages independently of immune response factors and trigger a non-phagocytic, low-inflammatory response. *J. Control Release* 366, 282–296. doi:10.1016/j.jconrel.2023.12.019

Boonyuen, S., Shanmugam, P., Ramachandran, R., Phromsatit, T., Teerawatananond, T., Tantayanon, S., et al. (2024). Exploring copper (II) porphyrin complexes and their derivatives for electrochemical analysis and biological assessment in the study of breast cancer (MCF-7) cell lines. *Environ. Res.* 250, 118489. doi:10.1016/j.envres.2024.118489

Cai, W., Wu, S., Lin, Z., Ming, X., Yang, X., Yang, M., et al. (2024). Hypoxia-induced BAP1 enhances erastin-induced ferroptosis in nasopharyngeal carcinoma by stabilizing H2A. *Cancer Cell Int.* 24 (1), 307. doi:10.1186/s12935-024-03494-z

Chargari, C., Maury, P., Texier, M., Genestie, C., Morice, P., Bockel, S., et al. (2024). Theragnostic gadolinium-based nanoparticles safely augment X-ray radiation effects in patients with cervical cancer. *ACS Nano* 18 (26), 16516–16529. doi:10.1021/acsnano. 3r12537

Chen, K., Preuss, A., Hackbarth, S., Wacker, M., Langer, K., and Roder, B. (2009). Novel photosensitizer-protein nanoparticles for photodynamic therapy: photophysical characterization and *in vitro* investigations. *J. Photochem Photobiol. B* 96 (1), 66–74. doi:10.1016/j.jphotobiol.2009.04.006

Daniel, G., Meirav, G., Noam, O., Tamar, B. K., Dvir, R., Ricardo, O., et al. (2023). Fast and accurate T(2) mapping using bloch simulations and low-rank plus sparse matrix decomposition. *Magn. Reson Imaging* 98, 66–75. doi:10.1016/j.mri.2023.01.007

Duan, X., Wang, P., He, L., He, Z., Wang, S., Yang, F., et al. (2024). Peptide-functionalized inorganic oxide nanomaterials for solid cancer imaging and therapy. *Adv. Mater* 36 (37), e2311548. doi:10.1002/adma.202311548

Fang, R. H., Gao, W., and Zhang, L. (2023). Targeting drugs to tumours using cell membrane-coated nanoparticles. *Nat. Rev. Clin. Oncol.* 20 (1), 33–48. doi:10.1038/s41571-022-00699-x

Generative AI statement

The author(s) declare that no Generative AI was used in the creation of this manuscript.

Any alternative text (alt text) provided alongside figures in this article has been generated by Frontiers with the support of artificial intelligence and reasonable efforts have been made to ensure accuracy, including review by the authors wherever possible. If you identify any issues, please contact us.

Publisher's note

All claims expressed in this article are solely those of the authors and do not necessarily represent those of their affiliated organizations, or those of the publisher, the editors and the reviewers. Any product that may be evaluated in this article, or claim that may be made by its manufacturer, is not guaranteed or endorsed by the publisher.

Supplementary material

The Supplementary Material for this article can be found online at: https://www.frontiersin.org/articles/10.3389/fnano.2025.1690060/full#supplementary-material

Garcia-Prada, C. D., Carmes, L., Atis, S., Parach, A., Bertolet, A., Jarlier, M., et al. (2023). Gadolinium-based nanoparticles sensitize ovarian peritoneal carcinomatosis to targeted radionuclide therapy. *J. Nucl. Med.* 64 (12), 1956–1964. doi:10.2967/jnumed. 123.265418

Gkotsis, D. E., Bherwani, A., Kapsalaki, E. Z., Bishop, C. J., and Schwarz, A. J. (2025). Contrast agent-specific parameter optimization for T1-Weighted fast spoiled gradient echo imaging: use cases for gadoterate meglumine and gadobutrol at 1.5T and 3.0T. *Invest. Radiol.* 60 (11), 791–801. doi:10.1097/RLI.000000000001205

Guerassimoff, L., Ferrere, M., Van Herck, S., Dehissi, S., Nicolas, V., De Geest, B. G., et al. (2024). Thermosensitive polymer prodrug nanoparticles prepared by an all-aqueous nanoprecipitation process and application to combination therapy. *J. Control Release* 369, 376–393. doi:10.1016/j.jconrel.2024.03.049

Hammond, J., Richards, C. J., Ko, Y., Jonker, T., Aberg, C., Roos, W. H., et al. (2025). Membrane fusion-based drug delivery liposomes transiently modify the material properties of synthetic and biological membranes. *Small* 21 (12), e2408039. doi:10.1002/smll.202408039

Haroon, H. B., Hunter, A. C., Farhangrazi, Z. S., and Moghimi, S. M. (2022). A brief history of long circulating nanoparticles. *Adv. Drug Deliv. Rev.* 188, 114396. doi:10. 1016/j.addr.2022.114396

Huang, S. Y., Gong, S., Zhao, Y., Ye, M. L., Li, J. Y., He, Q. M., et al. (2024). PJA1-mediated suppression of pyroptosis as a driver of docetaxel resistance in nasopharyngeal carcinoma. *Nat. Commun.* 15 (1), 5300. doi:10.1038/s41467-024-49675-2

Hvattum, E., Normann, P. T., Jamieson, G. C., Lai, J. J., and Skotland, T. (1995). Detection and quantitation of gadolinium chelates in human serum and urine by high-performance liquid chromatography and post-column derivatization of gadolinium with Arsenazo III. *J. Pharm. Biomed. Anal.* 13 (7), 927–932. doi:10.1016/0731-7085(95) 01311-8

Jin, G. Q., Chau, C. V., Arambula, J. F., Gao, S., Sessler, J. L., and Zhang, J. L. (2022). Lanthanide porphyrinoids as molecular theranostics. *Chem. Soc. Rev.* 51 (14), 6177–6209. doi:10.1039/d2cs00275b

Lechuga, M., Fernandez-Serrano, M., Rios, F., Fernandez-Arteaga, A., and Jimenez-Robles, R. (2022). Environmental impact assessment of nanofluids containing mixtures of surfactants and silica nanoparticles. *Environ. Sci. Pollut. Res. Int.* 29 (56), 84125–84136. doi:10.1007/s11356-022-21598-9

Lee, P. J., Sui, Y. H., Liu, T. T., Tsang, N. M., Huang, C. H., Lin, T. Y., et al. (2022). Epstein-Barr viral product-containing exosomes promote fibrosis and nasopharyngeal

carcinoma progression through activation of YAP1/FAPα signaling in fibroblasts. J. Exp. Clin. Cancer Res. 41 (1), 254. doi:10.1186/s13046-022-02456-5

- Li, W., Lam, S., Wang, Y., Liu, C., Li, T., Kleesiek, J., et al. (2024a). Model generalizability investigation for GFCE-MRI synthesis in NPC radiotherapy using multi-institutional patient-based data normalization. *IEEE J. Biomed. Health Inf.* 28 (1), 100–109. doi:10.1109/JBHI.2023.3308529
- Li, W., Zhao, D., Zeng, G., Chen, Z., Huang, Z., Lam, S., et al. (2024b). Evaluating virtual contrast-enhanced magnetic resonance imaging in nasopharyngeal carcinoma radiation therapy: a retrospective analysis for primary gross tumor delineation. *Int. J. Radiat. Oncol. Biol. Phys.* 120 (5), 1448–1457. doi:10.1016/j.ijrobp.2024.06.015
- Li, W., Liang, L., Liu, S., Zeng, F., Cao, J., Lei, Y., et al. (2025). CD38 inhibits ferroptosis to promote radiotherapy resistance in nasopharyngeal carcinoma by competitively binding to TRIM21 to stabilize SLC7A11 protein. *Int. J. Biol. Macromol.* 317 (Pt 2), 144742. doi:10.1016/j.ijbiomac.2025.144742
- Liang, Y. L., Liu, X., Shen, L. F., Hu, G. Y., Zou, G. R., Zhang, N., et al. (2025). Adjuvant PD-1 blockade with camrelizumab for nasopharyngeal carcinoma: the DIPPER randomized clinical trial. *JAMA* 333 (18), 1589–1598. doi:10.1001/jama. 2025.1132
- Lin, H., Tong, Q., Xu, J., Li, T., Yang, A., Sun, J., et al. (2023). An "IgG-hitchhiking" approach for rapid tumor accumulation and clearance of photosensitizers. *J. Control Release* 356, 242–255. doi:10.1016/j.jconrel.2023.02.026
- Liu, S., Jiang, Y., Liu, P., Yi, Y., Hou, D., Li, Y., et al. (2023). Single-Atom gadolinium nano-contrast agents with high stability for tumor T(1) magnetic resonance imaging. *ACS Nano*. 17 (9), 8053–8063. doi:10.1021/acsnano.2c09664
- Liu, D., Wang, H., Yang, W., Bai, Y., Wu, Z., Cui, T., et al. (2025). One-dose bioorthogonal gadolinium nanoprobes for prolonged radiosensitization of tumor. *Small* 21 (15), e2500504. doi:10.1002/smll.202500504
- Looi, C. K., Loo, E. M., Lim, H. C., Chew, Y. L., Chin, K. Y., Cheah, S. C., et al. (2024). Revolutionizing the treatment for nasopharyngeal cancer: the impact, challenges and strategies of stem cell and genetically engineered cell therapies. *Front. Immunol.* 15, 1484535. doi:10.3389/fimmu.2024.1484535
- Luo, Y., Wu, H., Feng, C., Xiao, K., Yang, X., Liu, Q., et al. (2017). "One-pot" fabrication of highly versatile and biocompatible Poly(vinyl alcohol)-porphyrin-based nanotheranostics. *Theranostics* 7 (16), 3901–3914. doi:10.7150/thno.20190
- Luo, Q., Liu, J., Ma, Q., Xu, S., and Wang, L. (2023). Single-atom Gd nanoprobes for self-confirmative MRI with robust stability. *Small* 19 (23), e2206821. doi:10.1002/smll. 202206821
- Martynov, A. G., Horii, Y., Katoh, K., Bian, Y., Jiang, J., Yamashita, M., et al. (2022). Rare-earth based tetrapyrrolic sandwiches: chemistry, materials and applications. *Chem. Soc. Rev.* 51 (22), 9262–9339. doi:10.1039/d2cs00559j
- Mohammed, S., Kuzmenko, I., and Gadikota, G. (2021). Reversible assembly of silica nanoparticles at water-hydrocarbon interfaces controlled by SDS surfactant. *Nanoscale* 14 (1), 127–139. doi:10.1039/d1nr06807e
- Moloudi, K., Khani, A., Najafi, M., Azmoonfar, R., Azizi, M., Nekounam, H., et al. (2023). Critical parameters to translate gold nanoparticles as radiosensitizing agents

- into the clinic. Wiley Interdiscip. Rev. Nanomed Nanobiotechnol 15 (6), e1886. doi:10. 1002/wnan.1886
- Priovoulos, N., Andersen, M., Dumoulin, S. O., Boer, V. O., and Van Der Zwaag, W. (2023). High-resolution motion-corrected 7.0-T MRI to derive morphologic measures from the human cerebellum *in vivo. Radiology* 307 (2), e220989. doi:10.1148/radiol. 220989
- Shi, Z., Zeng, Y., Luo, J., Wang, X., Ma, G., Zhang, T., et al. (2024). Endogenous magnetic lipid droplet-mediated cascade-targeted sonodynamic therapy as an approach to reversing breast cancer multidrug resistance. *ACS Nano* 18 (42), 28659–28674. doi:10.1021/acsnano.4c05938
- Siak, P. Y., Heng, W. S., Teoh, S. S. H., Lwin, Y. Y., and Cheah, S. C. (2023). Precision medicine in nasopharyngeal carcinoma: comprehensive review of past, present, and future prospect. *J. Transl. Med.* 21 (1), 786. doi:10.1186/s12967-023-04673-8
- Sun, H., Cai, H., Xu, C., Zhai, H., Lux, F., Xie, Y., et al. (2022). AGuIX nanoparticles enhance ionizing radiation-induced ferroptosis on tumor cells by targeting the NRF2-GPX4 signaling pathway. *J. Nanobiotechnology* 20 (1), 449. doi:10.1186/s12951-022-01654-9
- Wang, D., Yan, S., Sun, J., Xia, X., Pan, Z., Liu, Z., et al. (2024). Fluoropolymer-Gadolinium(III) hybrids for photoactivatable dual-mode T(1)-Weighted (1)H MRI and (19)F MRI contrast agents. ACS Macro Lett. 13 (10), 1286–1292. doi:10.1021/acsmacrolett.4c00459
- Wang, K., Jiang, S., Wang, W., Chen, W., and Kai, T. (2025). Dual-miRNA guided *in-vivo* imaging and multimodal nanomedicine approaches for precise hepatocellular carcinoma differentiation and synergistic cancer theranostics using DNA hairpins and dual-ligand functionalized zirconium-MOF nanohybrids. *Biomaterials* 321, 123330. doi:10.1016/j.biomaterials.2025.123330
- Wu, L., Jiang, M., Chu, C., Luo, T., Hui, Y., Zhou, W., et al. (2024). Transformation of black phosphorus through lattice reconstruction for NIR-II-Responsive cancer therapy. *Adv. Sci. (Weinh)* 11 (3), e2305762. doi:10.1002/advs.202305762
- Youden, B., Wang, F., Zhang, X., Curry, D., Majtenyi, N., Shaaer, A., et al. (2022). Degradable multifunctional gold-liposomes as an all-in-one theranostic platform for image-guided radiotherapy. *Int. J. Pharm.* 629, 122413. doi:10.1016/j.ijpharm.2022. 122413
- Zhang, X., Wang, X., Li, Z., Du, J., Xiao, X., Pan, D., et al. (2023). Lactose-modified enzyme-sensitive branched polymers as a nanoscale liver cancer-targeting MRI contrast agent. *Nanoscale* 15 (2), 809–819. doi:10.1039/d2nr04020d
- Zhang, J., Yuan, C., Kong, L., Zhu, F., Yuan, W., Zhang, J., et al. (2024). H-ferritin-nanocaged gadolinium nanoparticles for ultra-sensitive MR molecular imaging. *Theranostics* 14 (5), 1956–1965. doi:10.7150/thno.93856
- Zhang, R., Shen, Y., Zhou, X., Li, J., Zhao, H., Zhang, Z., et al. (2025). Hypoxia-tropic delivery of nanozymes targeting transferrin receptor 1 for nasopharyngeal carcinoma radiotherapy sensitization. *Nat. Commun.* 16 (1), 890. doi:10.1038/s41467-025-56134-z
- Zhdanova, K. A., Ivantsova, A. V., Vyalba, F. Y., Usachev, M. N., Gradova, M. A., Gradov, O. V., et al. (2023). Design of A3B-Porphyrin conjugates with terpyridine as potential Theranostic agents: synthesis, complexation with Fe(III), Gd(III), and photodynamic activity. *Pharmaceutics* 15 (1), 269. doi:10.3390/pharmaceutics15010269